Fossil vs. non-fossil CO sources in the US: New airborne constraints from ACT-America and GEM

Andres Gonzalez[1], Dylan B. Millet[1], Xueying Yu[1], Kelley C. Wells[1], Timothy J. Griffis[1], Bianca C. Baier[2], Patrick Campbell[3], Yonghoon Choi[4], Joshua Paul DiGangi[5], Alexander Gvakharia[6], Hannah Selene Halliday[7], Eric A. Kort[6], Kathryn McKain[8], John B. Nowak[5], and Genevieve Plant[9]

[1]University of Minnesota
[2]University of Colorado Boulder
[3]George Mason University
[4]Science Systems and Applications, INC.
[5]NASA Langley Research Center
[6]University of Michigan-Ann Arbor
[7]EPA
[8]National Oceanic and Atmospheric Administration (NOAA)
[9]University of Michigan

November 24, 2022

Abstract

Carbon monoxide (CO) is an ozone precursor, oxidant sink, and widely-used pollution tracer. The importance of anthropogenic versus other CO sources in the US is uncertain. Here we interpret extensive airborne measurements with an atmospheric model to constrain US fossil and non-fossil CO sources. Measurements reveal a low bias in the simulated CO background and a 30% overestimate of US fossil CO emissions in the 2016 National Emissions Inventory. After optimization we apply the model for source partitioning. During summer, regional fossil sources account for just 9-16% of the sampled boundary layer CO, and 32-38% of the North American enhancement-complicating use of CO as a fossil fuel tracer. The remainder predominantly reflects biogenic hydrocarbon oxidation plus fires. Fossil sources account for less domain-wide spatial variability at this time than non-fossil and background contributions. The regional fossil contribution rises in other seasons, and drives ambient variability downwind of urban areas.

Fossil vs. non-fossil CO sources in the US: New airborne constraints from ACT-America and GEM

Andres Gonzalez[1], Dylan B. Millet[1], Xueying Yu[1], Kelley C. Wells[1], Timothy J. Griffis[1], Bianca C. Baier[2,3], Patrick C. Campbell[4,5,6], Yonghoon Choi[7], Joshua P. DiGangi[7], Alexander Gvakharia[8], Hannah Halliday[7], Eric A. Kort[8], Kathryn McKain[2,3], John Nowak[7], and Genevieve Plant[8]

[1]Department of Soil, Water, and Climate, University of Minnesota, Saint Paul, MN, USA. [2]Cooperative Institute for Research in Environmental Sciences (CIRES), University of Colorado, Boulder, CO, USA. [3]Global Monitoring Laboratory, National Oceanic and Atmospheric Administration, Boulder, CO, USA. [4]Center for Spatial Information Science and Systems, George Mason University, Fairfax, VA, USA. [5]Cooperative Institute for Satellite Earth System Studies (CISESS).[6]Air Resources Laboratory, National Oceanic and Atmospheric Administration, College Park, MD, USA. [7]NASA Langley Research Center, Hampton, VA, USA. [8]Department of Climate and Space Sciences and Engineering, University of Michigan, Ann Arbor, MI, USA.

Corresponding author: Dylan Millet (dbm@umn.edu)

Key Points:

- We interpret an ensemble of airborne measurements with the GEOS-Chem model to constrain US fossil fuel and non-fossil CO sources
- Measurements reveal an approximate 30% overestimate of US fossil fuel CO emissions in the National Emissions Inventory
- During summer regional fossil fuel sources account for just 9-16% of total boundary layer CO over eastern North America

Abstract

Carbon monoxide (CO) is an ozone precursor, oxidant sink, and widely-used pollution tracer. The importance of anthropogenic versus other CO sources in the US is uncertain. Here we interpret extensive airborne measurements with an atmospheric model to constrain US fossil and non-fossil CO sources. Measurements reveal a low bias in the simulated CO background and a 30% overestimate of US fossil CO emissions in the 2016 National Emissions Inventory. After optimization we apply the model for source partitioning. During summer, regional fossil sources account for just 9-16% of the sampled boundary layer CO, and 32-38% of the North American enhancement—complicating use of CO as a fossil fuel tracer. The remainder predominantly reflects biogenic hydrocarbon oxidation plus fires. Fossil sources account for less domain-wide spatial variability at this time than non-fossil and background contributions. The regional fossil contribution rises in other seasons, and drives ambient variability downwind of urban areas.

Plain Language Summary

Carbon monoxide (CO) is an air pollutant that is emitted from fossil fuel combustion and from forest and agricultural fires. CO is also produced in the atmosphere through the oxidation of hydrocarbons from both natural and human-caused sources. US fossil fuel CO emissions have been declining in recent years, and their current importance relative to other regional sources is uncertain. Here, we interpreted a large group of aircraft-based CO measurements with a high-resolution atmospheric model to better quantify US fossil and non-fossil fuel CO sources over the eastern half of the US. We find that US fossil fuel CO emissions in the 2016 National Emissions Inventory are overestimated by approximately 30%. Furthermore, during summer regional fossil fuel sources account for only a small fraction of the CO over North America compared to the background concentrations already present in air entering North America, and compared to the regional source from natural hydrocarbon oxidation. This complicates the use of CO as a tracer for estimating fossil fuel sources of other pollutants such as carbon dioxide.

1 Introduction

Carbon monoxide (CO) is the largest sink of atmospheric hydroxyl (OH) radicals (Müller et al., 2018) and a major tropospheric ozone precursor (Hu et al., 2017). It is emitted from fossil fuel and biomass combustion and is also indirectly produced from the oxidation of methane and non-methane volatile organic compounds (VOCs). CO removal occurs mainly via reaction with OH, forming atmospheric carbon dioxide (CO_2) at an annual rate equivalent to ~10% of the global fossil fuel source (Duncan et al., 2007; Friedlingstein et al., 2019). As a result of its oxidative effects and their feedbacks, CO has a global warming potential approximately 5× that of CO_2 on a 100-year timescale (Shindell et al., 2009).

According to the National Emissions Inventory Collaborative (NEIC) Emissions Modeling Platform, based on the US Environmental Protection Agency (EPA) National Emissions Inventory (NEI), US CO emissions totaled ~55 Tg in 2016, with fossil fuel and biomass burning emissions accounting for 41 Tg and 14 Tg, respectively (NEIC, 2019). Fossil fuel sources in the inventory are predominantly mobile (on-road: 18 Tg; non-road: 10 Tg) and in the case of on-road emissions, mainly (90%) due to non-diesel light-duty vehicles. Gasoline combustion similarly accounts for the majority (80%) of the estimated non-road mobile source (NEI, 2014). Annual fossil fuel CO emissions in the NEI decreased by approximately 50 Tg/year from 2000-2016, driven by a nearly 70% drop in the estimated mobile source (EPA, 2019).

CO has traditionally been used as a fossil fuel tracer to diagnose anthropogenic sources of CO_2 and other species (e.g., Cheng et al., 2018; Halliday et al., 2019; Nathan et al., 2018; Super et al., 2017). In the US, however, the dramatic decline in transportation-related emissions (Gaubert et al., 2017; NEI, 2018; Parrish, 2006) means that non-fossil fuel CO sources are increasingly important. For example, Hudman et al. (2008) estimated that VOC oxidation (predominantly from biogenic precursors) was a two-fold larger CO source than direct combustion emissions over the US during summer 2004. Furthermore, previous NEI versions have been shown to overestimate US anthropogenic CO emissions by as much as 60% (Fujita et al., 2012; Kim et al., 2013; Salmon et al., 2018; Brioude et al., 2011; Brioude et al., 2013; Plant et al., 2019), so the non-fossil fuel CO fraction may be even greater than suggested by current inventories.

Together, the large recent emission trends and demonstrated inventory biases imply significant uncertainty in the current CO budget over North America. Two airborne measurement campaigns conducted from 2016-2019 with widespread, multi-seasonal coverage over the eastern half of the US provide new constraints for addressing this issue: the Atmospheric Carbon and Transport (ACT)-America mission, with 5 dual-aircraft deployments across three US regions (Davis et al., 2021), and the Greenhouse Emissions in the Midwest (GEM) mission with 3 deployments across the US Upper Midwest (Yu et al., 2020; 2021). Here, we employ the GEOS-Chem chemical transport model (CTM) to interpret these datasets in terms of their implications for fossil fuel versus non-fossil and primary versus secondary CO sources over the US.

2 Methods

2.1 Aircraft Measurements

Figure 1 shows flight-tracks for the ACT-America and GEM airborne deployments used here. ACT-America took place during summer 2016 (ACT1; see Table S1), winter 2017 (ACT2), fall 2017 (ACT3), spring 2018 (ACT4), and summer 2019 (ACT5) (Davis et al., 2018; Davis et al., 2021). Each deployment featured measurements aboard two aircraft (C-130 Hercules: 487 flight hours; Beechcraft B200 King Air: 513 flight hours) across the US Midwest, Northeast, and South. Sampling altitudes ranged from 0.1-8.7 km above ground level (AGL); only data below 8 km AGL are employed here. Airborne CO measurements were also performed for the first two GEM campaigns over the US Upper Midwest during summer 2017 (GEM1) and winter 2018 (GEM2). Measurements took place on a Mooney aircraft (76 flight hours) from 0.1 to 2.2 km AGL (Yu et al., 2020; Yu et al. 2021). We employ data from ACT1-ACT4 for CO source estimation and reserve ACT5, GEM1 and GEM2 for independent evaluation of the results.

ACT-America CO dry-air mole fraction measurements used here were performed in-situ by wavelength-scanned cavity ring-down spectroscopy (CRDS; Picarro G2401-m) with ±5 ppb estimated uncertainty (DiGangi et al., 2021; Wei et al., 2021). Additional CO measurements were obtained during ACT-America via air samples collected on-board both aircraft with Programmable Flask Packages (PFP) (Baier et al., 2020; Wei 2021; Davis et al., 2018). An intercomparison of the C-130-H and B-200 Picarro datasets using the PFP observations as transfer standard shows no significant difference (Figure S1) and we treat them here as a single statistical ensemble. GEM CO measurements were performed by continuous-wave tunable infrared laser absorption spectrometry (Aerodyne CW-TILDAS) with ±1 ppb estimated uncertainty (Gvakharia et al., 2018; Millet et al., 2019). In-situ measurements for ACT and GEM were made at 0.4 Hz and we use 1-minute averaged data in analyses that follow.

We also employ airborne CO measurement over the remote Pacific from the Atmospheric Tomography Mission (ATom) (Wofsy et al., 2018) to evaluate and adjust the chemical boundary conditions used in the nested GEOS-Chem simulations (Section 2.2). ATom featured pole-to-pole sampling from 0.2-12 km altitude during four separate deployments; CO measurements used here were collected using the NOAA Picarro instrument with estimated ±3.6 ppb uncertainty (Chen et al., 2013). ATom1 (Northern Hemisphere summer 2016), ATom2 (winter 2017), ATom3 (fall 2017) and ATom4 (spring 2018) overlap temporally with ACT1-ACT4, respectively, and are applied for correction accordingly. ATom1 data is further used for ACT5 and GEM1 background correction, and ATom2 data for GEM2 background correction, given their matching seasonal coverage. Correction procedures are explained below. All datasets are calibrated on the WMO X2014A scale.

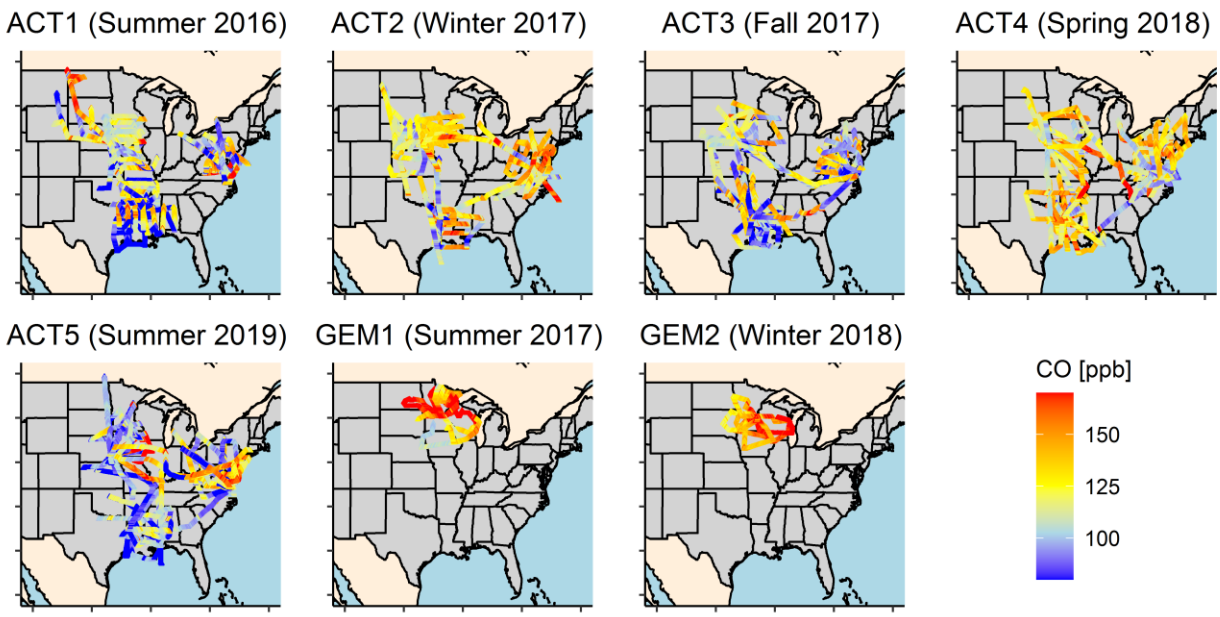

Figure 1: ACT-America and GEM flight-tracks colored by observed CO mixing ratios.

2.2 GEOS-Chem Simulations

We interpret the above airborne datasets using a GEOS-Chem (v12.6.3; doi:10.5281/zenodo.3552959) simulation nested at 0.25° × 0.3125° (latitude × longitude) resolution over North America (60°-130°W, 9.75°-60°N) with 47 vertical layers (Figure S2). Model runs are driven by GEOS-FP meteorological data from NASA GMAO (Lucchesi, 2013), and employ timesteps of 10-min (transport, convection) and 20-min (emissions, chemistry). A 1-month nested spinup is used for initialization.

Chemical boundary conditions (3-hourly) for the nested model domain are obtained from global simulations at 2° × 2.5° and bias-corrected using a latitude-dependent fit of model-measurement 0.1 quantile differences (6° latitude bins from 66°S-54°N) along the ATom flight-tracks over the remote Pacific (Figure S3). As described later, we also perform a sensitivity analysis without this boundary condition correction as one test of our results.

We use tagged tracers (Fisher et al., 2017) to track contributions to ambient CO from direct and indirect CO sources within the North American domain shown in Figure S2 and from the chemical boundary conditions (CO_{bc}). Tagged direct sources include US on-road mobile emissions (CO_{usrd}), US non-road mobile emissions (CO_{usnr}), other US anthropogenic sources (CO_{usot}), non-US anthropogenic emissions (CO_{camx}; from Canada and Mexico) and wildfires plus agricultural burning (CO_{bb}). We separately track secondary CO (CO_{prod}) from the oxidation of biogenic VOCs (CO_{prod_bio}), anthropogenic VOCs (CO_{prod_anth}), and other precursors (CO_{prod_oth}; methane plus pyrogenic VOCs) occurring within the North American domain. CO production and removal rates are computed using archived fields from full-chemistry simulations at 2° × 2.5°; secondary contributions from biogenic and anthropogenic VOCs are derived from runs with the corresponding emissions perturbed by 10%.

Global anthropogenic emissions in the model are from the Community Emissions Data System (Hoesly et al., 2018) overwritten for the US by the 2016 EPA NEI (NEIC2016v1; NEIC, 2019) and for Canada by the Air Pollutant Emission Inventory (APEI, 2020). Biogenic emissions are from the Model of Emissions of Gases and Aerosols from Nature (MEGANv2.1)

implemented as described by Hu et al. (2015), and biomass burning emissions use the Quick-Fire Emissions Dataset (Koster et al., 2015).

3 Results

3.1 Measured Versus Predicted CO over the Eastern and Central US

Figure 2a-g shows the mean vertical CO profiles measured during ACT1-ACT5 and GEM1-GEM2. Average concentrations during the ACT-America flights peak in the planetary boundary layer (PBL; defined here as $z < 2$ km) at ~120-125 ppb during summer and fall, and at ~140 ppb during spring and winter. Concentrations during GEM (which sampled farther north and predominantly within the PBL) are slightly higher. Aloft, we see free tropospheric ($z > 4$ km) concentrations ranging seasonally between ~80-90 ppb (summer) and ~100-110 ppb (winter).

Also shown in Figure 2a-g are the CO mixing ratios simulated by GEOS-Chem along the flight-tracks at the time of measurement, with the corresponding tagged-tracer source contributions. The base-case simulation successfully captures the relative vertical distribution of CO, but underestimates its abundance in all seasons except fall (ACT3). The magnitude of this low bias during spring, summer, and winter ranges from 9 ppb (averaged below 2 km) during spring for ACT4 to 48 ppb during summer for GEM1.

Transport from outside North America makes the largest contribution to ambient CO over the eastern half of the US in the GEOS-Chem base-case simulation (Figure 2a-g). This background varies little with altitude and changes seasonally in concert with the CO lifetime, from ~50 ppb in summer (for ACT1 and ACT5) to ~100 ppb in winter (for ACT2 and GEM2). We see from Figure 2 that the background contribution dominates total CO in the free troposphere (71-96% above 4 km, lowest in summer). At lower altitudes, regional CO sources play a larger role; nevertheless, the CO background still represents 55% (summer) to 78% (winter) of the total averaged model abundance below 2 km.

Figure 2h-n shows the base-case model partitioning of North American CO enhancements (i.e., excluding CO_{bc}, which is already present in air entering North America) during ACT-America and GEM. The regional secondary source is further partitioned into biogenic, anthropogenic, and other (methane + pyrogenic VOC) contributions. We see that secondary production accounts for a significant fraction of the predicted North American CO source, particularly during summer when, in the case of ACT1 and ACT5, it mainly arises from biogenic VOC oxidation. Primary emissions mainly reflect US anthropogenic sources (in turn dominated by on-road and off-road mobile emissions). GEM1, over the Upper Midwest, featured a larger contribution from biomass burning.

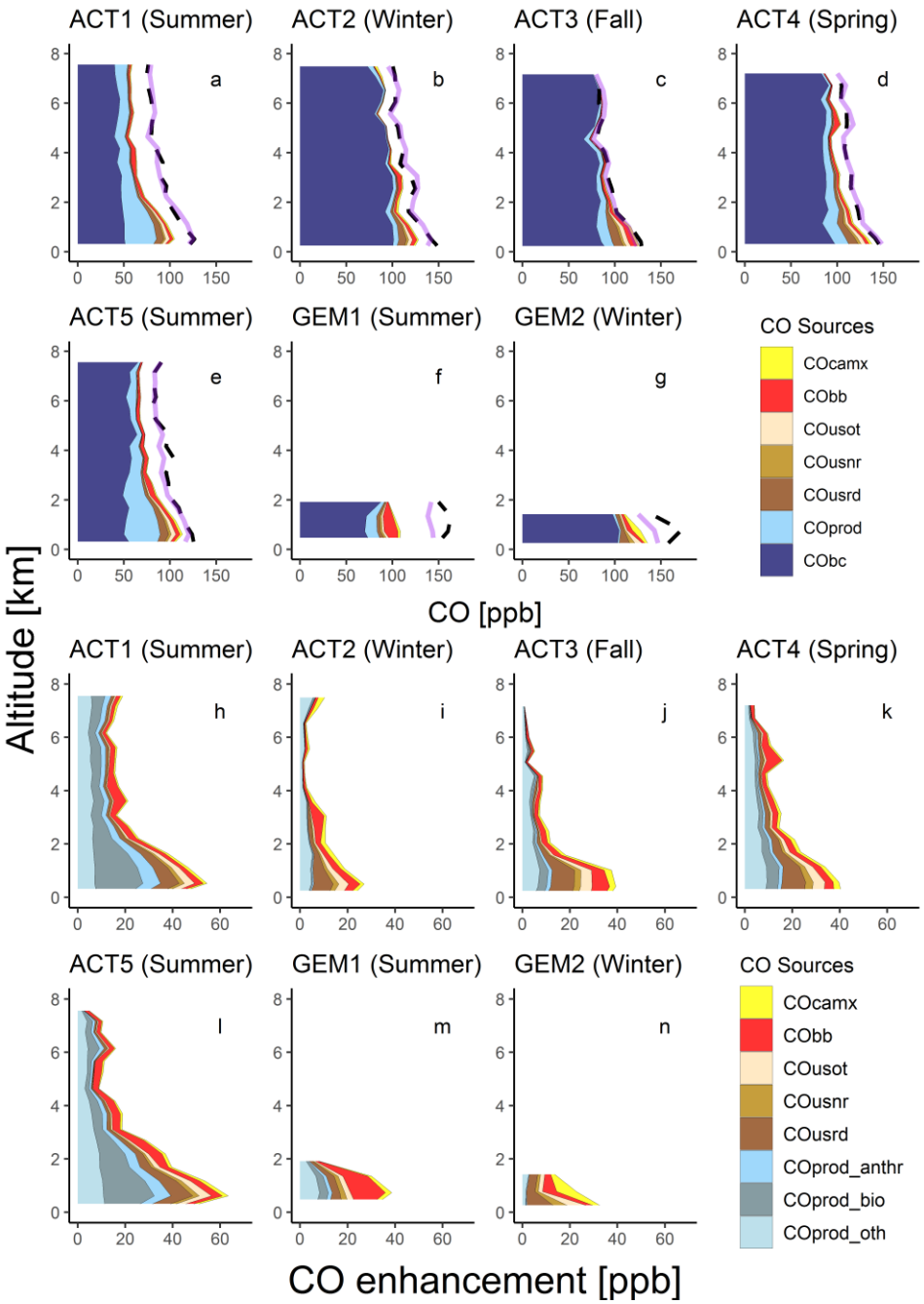

Figure 2: Mean CO profiles during ACT-America and GEM. Panels a-g compare observed CO mixing ratios (black dashed lines) with those predicted by the prior GEOS-Chem simulation (stacked color plots). Pink lines show simulated CO concentrations after source optimization. Panels h-n show the above-background source contributions based on the prior GEOS-Chem simulation. CO_{usrd}, CO_{usnr}, CO_{usot}: anthropogenic CO from US on-road, non-road, and other sources. CO_{camx}: anthropogenic CO emitted in Canada + Mexico. CO_{bb}: CO from North American biomass burning. CO_{prod}: CO photochemically produced over North America from the oxidation of biogenic VOCs (CO_{prod_bio}), anthropogenic VOCs (CO_{prod_anth}), and methane + biomass burning VOCs (CO_{prod_oth}). CO_{bc}: CO transported from outside North America.

3.2 CO Source Optimization

We next apply the base-case tagged tracer simulations discussed above to develop improved US CO source estimates based on the ACT-America observations. The optimization is performed separately for ACT1-ACT4 and consists of two steps. First, since background CO dominates the total free tropospheric abundance (Figure 2), we attribute the prior model bias aloft accordingly and correct the simulated CO_{bc} based on the mean >4 km model-measurement differences for each campaign. Given the vertical uniformity of CO_{bc} this correction is applied throughout the column and ranges from a factor of 1.0 during fall to 1.5 during summer.

Second, after subtracting this corrected background we derive top-down adjustments on regional CO sources by regressing the model tagged tracers against the observed above-background enhancements below 2 km AGL. Selected tracers are grouped for optimization to avoid multicollinearity and based on their relative abundance. During summer we thus optimize 1) direct CO emissions from US onroad, non-road mobile, and other anthropogenic sources ($\mathrm{CO}_{usnei} = \mathrm{CO}_{usrd} + \mathrm{CO}_{usnr} + \mathrm{CO}_{usot}$) and 2) regional secondary CO production from biogenic and anthropogenic VOCs ($\mathrm{CO}_{prod\_voc} = \mathrm{CO}_{prod\_bio} + \mathrm{CO}_{prod\_anth}$) as single variables based on the high cross-correlation (R = 0.92-0.98) among the grouped tracers. Other secondary production (CO_{prod_oth}) is not optimized as it is primarily from methane and implicitly corrected by the preceding background adjustment. CO sources from Canada and Mexico and from biomass burning each make up <18% of the above-background model abundance during ACT1-4 and are likewise not optimized. During other seasons the same procedure is used but without optimizing CO_{prod_voc} as it then accounts for <16% of the mean above-background enhancements. A sensitivity test described later explores how how the choice of tracer groups for optimization affects our results.

In this way we obtain seasonal top-down correction factors for the NEIC2016v1 US anthropogenic CO emissions, along with a top-down correction to the regional secondary source from biogenic + anthropogenic VOCs during summer. Results shown in Table 1 are consistent across the seasonal ACT-America campaigns in revealing a moderate NEI overestimate of US anthropogenic CO emissions, with coefficients ranging from 0.66 ± 0.05 to 0.79 ± 0.03 (here and below, stated uncertainties reflect bootstrapped 95% confident intervals). We find that secondary CO production from regional VOC oxidation is well-represented in the model, with a derived scale factor of 0.91 ± 0.03.

Figure 2 and Table 1 show that the optimization successfully minimizes the prior model bias, and either improves or maintains the prior model:measurement correlation. An exception is ACT3, where the prior simulation was already essentially unbiased (< 3 ppb) with high correlation. However, the posterior fit quality here is still comparable to that obtained in other seasons. In the following section, we apply a series of statistical and sensitivity analyses and independent data comparisons to further test the representativeness and robustness of these results.

Table 1. Seasonal CO source optimization[1]

	CO_{usnei}		CO_{prod_voc}		Intercept	VIF[2]	Mean bias (ppb)		RMSE[3] (ppb)		*R*	
	Scale factor	Mean (ppb)	Scale factor	Mean (ppb)			Prior	Post	Prior	Post	Prior	Post
ACT1 (summer)	0.66 ± 0.05	13.2	0.91 ± 0.03	25.4	-0.2 ± 0.3	3.1	17.6	-0.2	26.4	16.5	0.75	0.81
ACT2 (winter)	0.79 ± 0.03	12.77			1.8 ± 0.3		14.8	1.7	21.4	15.5	0.69	0.69
ACT3 (fall)	0.69 ± 0.03	16.77			5.5 ± 0.5		2.5	5.5	13.4	14.2	0.79	0.75
ACT4 (spring)	0.74 ± 0.02	16.94			-2.7 ± 0.4		8.8	-2.6	18.1	17.0	0.65	0.62

[1] Stated uncertainties reflect 95% confidence intervals computed through bootstrap resampling.
[2] Variance inflation factor.
[3] Root mean square error.

3.3 Uncertainty Analysis

The bootstrapped uncertainty estimates in Table 1 provide a first evaluation of the optimization results, showing that the individual scaling coefficients derived from ACT1-ACT4 are each statistically robust. The similar findings across ACT1-ACT4 provide a second piece of supporting evidence, as the deployments represent four separate datasets and independent source derivations that all lead to consistent results. Third, we see from Figure 2 and Table S2 that the CO source optimization (derived from ACT1-ACT4 data) strongly improves model performance versus independent airborne data from ACT5, GEM1, and GEM2, which were not employed in the optimization.

As a fourth test, we perform the CO source optimization separately for the two ACT-America aircraft. Table S3 shows that we arrive at the same conclusions when analyzing the B-200 and C-130 observations independently as opposed to treating them as a combined dataset. Specifically, we infer an NEI overestimate of US anthropogenic CO emissions in both cases, with derived scale factors spanning 0.54-0.87 (sensitivity tests) versus 0.66-0.79 (base analysis). The modest adjustment to the modeled secondary CO source from regional biogenic and anthropogenic VOCs is likewise independently supported by both airborne datasets (scale factors of 0.74-0.96 versus 0.91 in the base-case).

A fifth evaluation repeats the base-case optimization with alternate boundary conditions (CO_{bc}) for the nested model domain—i.e., employing the native model output for this purpose and omitting the ATom-based background adjustment (Section 2.2; Figure S3). Results in Table S4 show that scale factors derived in this way are statistically consistent with the base-case analysis. For a sixth and final test, we modify the tracer groupings used for optimization and instead derive ACT1-ACT4 scale factors for 1) CO_{usnei} and 2) the sum of all other regional source tracers. Results shown in Table S5 are again consistent with the base-case findings, with a slightly wider range for the CO_{usnei} scale factor (0.58-0.85) and a modestly degraded observational fit.

Overall, the above uncertainty tests all support our core findings, and we proceed to interpret the optimized results in terms of their implications for fossil fuel versus non-fossil, and primary versus secondary, CO sources over the US.

3.3.3 Optimized CO Source Contributions

Figure 3a-g shows the optimized primary and secondary North American contributions to ambient CO as sampled during ACT-America and GEM. We find that secondary production (mainly from biogenic VOCs) is the dominant summertime North American CO source for air masses sampled by ACT-America, accounting for ~70% of the total PBL enhancement. Secondary production is also significant at other times (e.g., 26-45% of the PBL enhancement during the fall, winter, and spring ACT-America campaigns) but then mainly reflects regional methane oxidation along with pyrogenic VOC oxidation. To the north, the importance of secondary CO over the Upper Midwest during GEM is significantly less (~7-40%)—reflecting lower biogenic VOC emissions and slower regional photochemistry. In total, photochemical CO sources contribute between 2 ppb (winter; GEM2) and 31 ppb (summer; ACT5) to the average sampled PBL enhancements, versus 13-25 ppb from primary emissions.

In Figure 3h-n we further partition the optimized CO abundance into fossil fuel versus non-fossil contributions. Here, fossil fuel sources include primary emissions plus secondary production from anthropogenic VOC, while non-fossil fuel sources include biogenic VOC oxidation plus biomass burning CO emissions. The remainder is from the oxidation of methane and of fire-derived VOCs. Results show that fossil fuel sources account for just 32-38% of the North American PBL CO enhancements sampled by ACT-America and GEM during summer, increasing to 48-49% during spring/fall and 57-84% during winter.

The findings above reveal the complications of using CO as an anthropogenic tracer, particularly during summer—as fossil fuel sources account for just 9-16% of the total PBL abundance, and 32-38% of the North American enhancement, during this season. However, for many applications (e.g., applying species:species correlations for source partitioning), source impacts on tracer variability can be more important than their absolute magnitude. For example, one might expect the secondary CO source to be relatively diffuse and that direct anthropogenic emissions would be a more important driver of ambient CO variability over the US.

To explore this expectation, Figures S4-S5 show the CO standard deviation by source category (based on the optimized GEOS-Chem simulation), for each airborne campaign in its entirety. In the summertime PBL sampled by ACT-America and GEM, the CO variability due to North American (primary + secondary) fossil fuel sources is substantially smaller (7-10 ppb) than that associated with background (15-21 ppb) and regional non-fossil fuel (11-15 ppb) contributions. In other seasons, regional fossil fuel emissions drive as much or more of the CO variability than non-fossil sources, but (except in the case of GEM) this variability is still smaller than that associated with the CO background.

The characterization above, treating each ACT-America and GEM campaign as a single statistical datasert, mainly describes spatial patterns of CO variability across the eastern half of the US as a whole. If we instead apply the optimized model to map the drivers of temporal CO variability (Figures S6-S10), we observe in all seasons a dominant role for fossil fuel emissions in and downwind of most urbanized areas. A similar finding applies for fires in specific affected regions. Temporal variability associated with secondary CO, manifesting most strongly in summer, is relatively low over much of the US Southeast where precursor VOC emissions are highest but is elevated around the periphery of this region (e.g., Figures S6, S11, S16). We attribute this to transport-driven effects at the edges of a large and diffuse source region (Figures S11-S15). In other seasons, temporal variability associated with secondary CO is small, with

fossil fuel emissions, biomass burning, and background CO playing more important roles (Figure S7-S9).

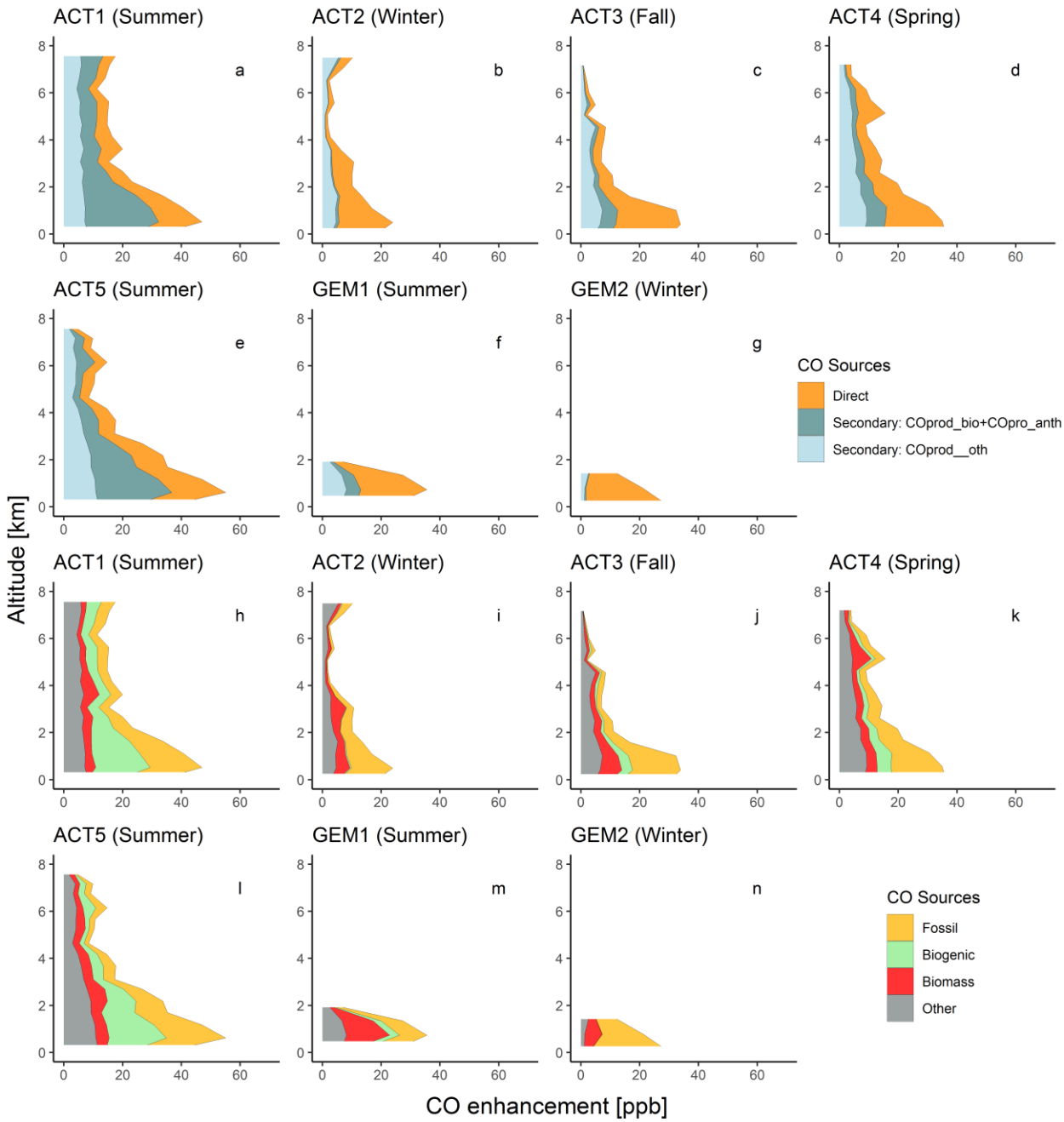

Figure 3: Observationally-constrained CO source attribution over the eastern US. Plotted are the mean above-background CO profiles from the optimized GEOS-Chem simulation along the aircraft flight-tracks. Panels a-g partition the regional CO enhancements into direct and secondary components. Direct sources include: anthropogenic CO from US on-road (CO_{usrd}), non-road (CO_{usnr}), and other sources (CO_{usot}), anthropogenic CO emitted in Canada + Mexico (CO_{camx}), and biomass burning CO (CO_{bb}). Secondary sources (CO_{prod}) include oxidation of

biogenic + anthropogenic VOC ($\mathrm{CO}_{prod\_bio} + \mathrm{CO}_{prod\_anth}$) and of methane + biomass burning VOCs (CO_{prod_oth}). Panels h-n partition the regional CO enhancements into fossil fuel (direct + secondary), biogenic (exclusively secondary), biomass burning (direct), and other (mainly methane oxidation, plus secondary biomass burning) contributions.

4 Conclusions

We applied measurements from 13 airborne campaigns to develop new constraints on CO sources over the central and eastern US. Data were collected over 1,000 flight hours across all seasons, representing the densest airborne dataset yet for CO source quantification over North America. Campaign-average PBL (< 2 km) mixing ratios ranged from 121 (summer) to 158 ppb (winter). Interpreting this dataset with a high-resolution version of the GEOS-Chem CTM driven by the US EPA's NEIC2016v1 inventory, we find that the model accurately captures the observed CO vertical profile shape but underestimates its abundance (by 9-48 ppb) in all seasons except fall. This disparity partly reflects a bias in the model CO background, and after correction we infer an NEI overestimate of fossil fuel CO emissions, with a derived top-down adjustment factor of 0.72 (0.54-0.87; best estimate and uncertainty range across all sensivity tests and seasons). For comparison, the US EPA estimates that national fossil fuel CO emissions decreased by 8% from 2016-2019 (EPA, 2019). Our top-down estimate for the secondary CO source from North American VOC emissions agrees well with the prior model value, with a derived scale factor of 0.91 (0.74-0.96). If the above comparisons are nationally representative, the implied US fossil fuel CO source for 2016-2019 was 29 (22-36) Tg/y, compared to the prior NEIC2016v1 estimate of 41 Tg/y (for 2016).

After optimizing the model based on the airborne constraints, we find that the CO background represents on average 55-78% of the PBL CO sampled during the aircraft campaigns. During summer, North American fossil fuel sources account for only 9-16% of the sampled PBL CO, and 32-38% of the enhancements associated with regional sources. Non-fossil sources from biogenic VOC oxidation and fires account for 40-45% of the above-background enhancements at this time, with the remainder mainly from regional methane oxidation. In other seasons, however, fossil fuel emissions are the largest regional source of CO.

Application of CO as a fossil fuel tracer is challenged by the fact that, during the growing season, such sources account for only a modest fraction of the CO burden and its spatial variability across the US. However, in and near most urbanized regions the temporal variability in CO is still dominated by fossil fuel sources. The number of locations where this remains the case will likely diminish, as US fossil fuel CO emissions are expected to continue declining with future vehicle emission regulations, advanced emission after-treatment technologies, and fleet electrification (Winkler et al., 2018; Nopmongcol et al., 2017).

Acknowledgments, Samples, and Data.

This work was supported by NASA (grant #NNX17AK18G) and the Minnesota Supercomputing Institute. The ACT-America, GEM, and ATom datasets are publicly available at https://doi.org/10.3334/ORNLDAAC/1593, https://doi.org/10.13020/f50r-zh70, and https://doi.org/10.3334/ORNLDAAC/1732. GEOS-Chem model code is publicly available at http://www.geos-chem.org. This work was also supported in part by NSF grant #1650682

(E.AK., A.G., G.P.) and by NASA grants #NNX15AJ06G (B.C.B), #NNX15AJ23G (ATom campaign), and #80NSSC18K1393 (X.Y.). We thank Ken Davis, Zach Barkley, and the entire ACT-America team for their contributions.

References

ACT-America, or Atmospheric Carbon and Transport (2019). Retrieved September 22, 2020 from https://act-america.larc.nasa.gov/science/

APEI (2020). Canada's Air Pollutant Emissions Inventory. Retrieved April 10, 2020 from https://open.canada.ca/data/en/dataset/fa1c88a8-bf78-4fcb-9c1e-2a5534b92131

Baier, B. C., Sweeney, C., Choi, Y., Davis, K. J., DiGangi, J. P., Feng, S., et al. (2020). Multispecies assessment of factors influencing regional CO_2 and CH_4 enhancements during the winter 2017 ACT-America campaign. *Journal of Geophysical Research: Atmospheres*, 125(2), doi:e2019JD031339.

Brioude, J., Kim, S.-W., Angevine, W. M., Frost, G. J., Lee, S.-H., McKeen, S. A., et al. (2011). Top-down estimate of anthropogenic emission inventories and their interannual variability in Houston using a mesoscale inverse modeling technique. *Journal of Geophysical Research: Atmospheres*, 116(D20 305). doi:10.1029/2011jd016215

Brioude, J., Angevine, W. M., Ahmadov, R., Kim, S. W., Evan, S., McKeen, S. A., et al. (2013). Top-down estimate of surface flux in the Los Angeles Basin using a mesoscale inverse modeling technique: assessing anthropogenic emissions of CO, NO_x and CO_2 and their impacts. *Atmospheric Chemistry and Physics*, 13(7), 3661-3677. doi:10.5194/acp-13-3661-2013

Chen, H., Karion, A., Rella, C. W., Winderlich, J., Gerbig, C., Filges, A., et al. (2013). Accurate measurements of carbon monoxide in humid air using the cavity ring-down spectroscopy (CRDS) technique. *Atmospheric Measurement Techniques*, *6*(4), 1031-1040. doi:10.5194/amt-6-1031-2013

Cheng, Y., Wang, Y., Zhang, Y., Crawford, J. H., Diskin, G. S., Weinheimer, A. J., & Fried, A. (2018). Estimator of surface ozone using formaldehyde and carbon monoxide concentrations over the eastern United States in summer. *Journal of Geophysical Research: Atmospheres*, *123*(14), 7642-7655. doi:10.1029/2018JD028452

Davis, K. J., Obland, M. D., Lin, B., Lauvaux, T., O'dell, C., Meadows, B., et al. (2018). ACT-America: L3 merged in situ atmospheric trace gases and flask data, Eastern USA. *ORNL DAAC*. doi:10.3334/ORNLDAAC/1593

Davis, K. J.,Browell, E.V., Feng, S., Lauvaux, T., Obland, M.D., Pal, S., et al .(2021).The Atmospheric carbon and transport (ACT) – America Mission. In review, *Bulletin American Meteorological Society*. doi:pdf/10.1002/essoar.10505721.1.

DiGangi, J. P., Choi, Y., Nowak, J. B., Halliday, H. S., Diskin, G. S., Feng, S., et al. (2021). Seasonal variability in local carbon dioxide combustion sources over the central and eastern US using airborne in-situ enhancement ratios. *Earth and Space Science Open Archive ESSOAr*. doi: 10.1002/essoar.10505716.1

Duncan, B. N., Logan, J. A., Bey, I., Megretskaia, I. A., Yantosca, R. M., Novelli, P. C., et al. (2007). Global budget of CO, 1988–1997: Source estimates and validation with a global model. *Journal of Geophysical Research*, 112, D22301 . doi:10.1029/2007jd008459

EPA (2019) Air Pollutant Emissions Trends Data. Retrieved September 18, 2020, from https://www.epa.gov/air-emissions-inventories/air-pollutant-emissions-trends-data

Fisher, J. A., Murray, L. T., Jones, D., & Deutscher, N. M. (2017). Improved method for linear carbon monoxide simulation and source attribution in atmospheric chemistry models illustrated using GEOS-Chem v9. *Geoscientific Model Development*, 10(11), 4129-4144. doi:10.5194/gmd-10-4129-2017

Friedlingstein, P., Jones, M., O'sullivan, M., Andrew, R., Hauck, J., Peters, G., et al. (2019). Global carbon budget 2019. *Earth System Science Data*, 11(4), 1783-1838. doi:10.5194/essd-11-1783-2019

Fujita, E. M., Campbell, D. E., Zielinska, B., Chow, J. C., Lindhjem, C. E., DenBleyker, A., et al. (2012). Comparison of the MOVES2010a, MOBILE6.2, and EMFAC2007 mobile source emission models with on-road traffic tunnel and remote sensing measurements. *Journal of the Air & Waste Management Association*, 62(10), 1134–1149. doi:10.1080/10962247.2012.699016

Gaubert, B., Worden, H. M., Arellano, A. F. J., Emmons, L. K., Tilmes, S., Barré, J., et al. (2017). Chemical feedback from decreasing carbon monoxide emissions. *Geophysical Research Letters*, 44(19), 9985–9995. doi:10.1002/2017gl074987

Gvakharia, A., Kort, E. A., Smith, M. L., & Conley, S. (2018). Testing and evaluation of a new airborne system for continuous N_2O, CO_2, CO, and H_2O measurements: the Frequent Calibration High-performance Airborne Observation System (FCHAOS). *Atmospheric Measurement Techniques*, *11*(11), 6059-6074. doi: 10.5194/amt-11-6059-2018

ESRL. Earth System Research Laboratories. Aircraft Program Methods (2020). Retrieved November 18, 2020 from https://www.esrl.noaa.gov/gmd/ccgg/aircraft/sampling.html

Halliday, H. S., DiGangi, J. P., Choi, Y., Diskin, G. S., Pusede, S. E., Rana, M., et al. (2019). Using short-term CO/CO_2 ratios to assess air mass differences over the Korean peninsula during KORUS-AQ. *Journal of Geophysical Research: Atmospheres*, 124(20), 10951–10972. doi:10.1029/2018jd029697

Hoesly, R. M., Smith, S. J., Feng, L., Klimont, Z., Janssens-Maenhout, G., Pitkanen, T., et al. (2018). Historical (1750-2014) anthropogenic emissions of reactive gases and aerosols from the Community Emission Data System (CEDS). *Geoscientific Model Development*, 11, 369-408. doi:10.5194/gmd-2017-43-supplement

Hu, L., Millet, D. B., Baasandorj, M., Griffis, T. J., Turner, P., Helmig, D., et al. (2015). Isoprene emissions and impacts over an ecological transition region in the US Upper Midwest inferred from tall tower measurements. *Journal of Geophysical Research: Atmospheres*, 120(8), 3553-3571. doi:10.1002/2014jd022732

Hu, L., Jacob, D. J., Liu, X., Zhang, Y., Zhang, L., Kim, P. S., et al. (2017). Global budget of tropospheric ozone: Evaluating recent model advances with satellite (OMI), aircraft (IAGOS), and ozonesonde observations. *Atmospheric Environment*, 167, 323–334. doi10.1016/j.atmosenv.2017.08.036

Hudman, R. C., Murray, L. T., Jacob, D. J., Millet, D. B., Turquety, S., Wu, S., et al (2008). Biogenic versus anthropogenic sources of CO in the United States. *Geophysical Research Letters*, 35(4). doi:10.1029/2007gl032393

Kim, S. Y., Millet, D. B., Hu, L., Mohr, M. J., Griffis, T. J., Wen, D., et al. (2013). Constraints on carbon monoxide emissions based on tall tower measurements in the U.S. upper midwest. *Environmental Science & Technology*, 130725095602007. doi:10.1021/es4009486

Koster, R. D., Darmenov, A. S., & da Silva, A. M. (2015). The Quick Fire Emissions Dataset (QFED): Documentation of Versions 2.1, 2.2 and 2.4. Volume 38; *Technical Report Series on Global Modeling and Data Assimilation.*

Lucchesi, R. (2013). File Specification for GEOS-5 FP, NASA GMAO Office Note, No. 4 (Version 1.0). *National Aeronautics and Space Administration, Goddard Space Flight Center, Greenbelt, Maryland, USA:* Available online at http://gmao. gsfc. nasa. gov/pubs

Millet, D.B., Conley, S.A., Gvakharia, A., Kort, E.A., Plant, G., Smith, M.L., and Yu.X. (2019). Airborne measurements from the GEM study. *Retrieved from the Data Repository for the University of Minnesota*, doi:10.13020/f50r-zh70.

Müller, J. F., Stavrakou, T., Bauwens, M., George, M., Hurtmans, D., Coheur, P. F., Clerbaux, C., & Sweeney, C. (2018). Top-down CO emissions based on IASI observations and hemispheric constraints on OH Levels. *Geophysical Research Letters*, 45(3), 1621–1629. doi:10.1002/2017gl076697

Nathan, B. J., Lauvaux, T., Turnbull, J. C., Richardson, S. J., Miles, N. L., & Gurney, K. R. (2018). Source sector attribution of CO_2 emissions using an urban CO/CO_2 Bayesian inversion system. *Journal of Geophysical Research: Atmospheres*, 123(23), 13-611. doi:10.1029/2018jd029231

National Emissions Inventory (NEI). (2014). Retrieved February 26, 2020, from https://edap.epa.gov/public/extensions/nei_report_2014/dashboard.html#sector-db

National Emissions Inventory Collaborative (NEIC) (2019). 2016beta Emissions Modeling Platform. Retrieved from http://views.cira.colostate.edu/wiki/wiki/10197.

Nopmongcol, U., Grant, J., Knipping, E., Alexander, M., Schurhoff, R., Young, et al. (2017). Air quality impacts of electrifying vehicles and equipment across the United States. *Environmental science & technology*, *51*(5), 2830-2837. doi: 10.1021/acs.est.6b04868

Oak Ridge National Laboratory Distributed Active Archive Center (ORNL DAAC)(2020). Retrieved February 21, 2020, from https://daac.ornl.gov/cgi-bin/dataset_lister.pl?p=37#:~:text=The%20ACT%2DAmerica%2C%20or%20Atmospheric,in%20the%20eastern%20United%20States.

Parrish, D. D. (2006). Critical evaluation of US on-road vehicle emission inventories. *Atmospheric Environment*, 40(13), 2288–2300. doi 10.1016/j.atmosenv.2005.11.033

Plant, G., Kort, E. A., Floerchinger, C., Gvakharia, A., Vimont, I., & Sweeney, C. (2019). Large fugitive methane emissions from urban centers along the U.S. East Coast. *Geophysical Research Letters*, 46, 8500–8507. doi:10.1029/2019GL082635

Salmon, O. E., Shepson, P. B., Ren, X., He, H., Hall, D. L., Dickerson, R. R., et al. (2018). Top-down estimates of NO_x and CO emissions from Washington, DC-Baltimore during the winter

campaign. *Journal of Geophysical Research: Atmospheres*, 123(14), 7705-7724. doi:10.1029/2018jd028539

Shindell, D. T., Faluvegi, G., Koch, D. M., Schmidt, G. A., Unger, N., & Bauer, S. E. (2009). Improved attribution of climate forcing to emissions. *Science*, 326(5953), 716-718. doi:10.1126/science.1174760

Super, I., van der Gon, H. D., Visschedijk, A. J. H., Moerman, M. M., Chen, H., Van der Molen, M. K., & Peters, W. (2017). Interpreting continuous in-situ observations of carbon dioxide and carbon monoxide in the urban port area of Rotterdam. *Atmospheric Pollution Research*, 8(1), 174–187. doi:10.1016/j.apr.2016.08.008

Wei Y., Shrestha R., Pal S., Gerken T., McNelis J., Singh D., et al. (2021). The ACT-America datasets: Description, Management and Delivery, *Earth Space Sci*, in review. https://www.essoar.org/doi/pdf/10.1002/essoar.10505692.1.

Winkler, S. L., Anderson, J. E., Garza, L., Ruona, W. C., Vogt, R., & Wallington, T. J. (2018). Vehicle criteria pollutant (PM, NO_x, CO, HCs) emissions: how low should we go?. *npj Climate and Atmospheric Science*, *1*(1), 1-5. doi:10.1038/s41612-018-0037-5

Wofsy, S.C., S. Afshar, H.M. Allen, E.C. Apel, E.C. Asher, B. Barletta, et al. (2018). ATom: merged atmospheric chemistry, trace gases, and aerosols. *ORNL DAAC*, Oak Ridge, Tennessee, USA. doi:10.3334/ORNLDAAC/1581

Yu, X., Millet, D. B., Wells, K. C., Griffis, T. J., Chen, X., Baker, J. M., et al. (2020). Top-down constraints on methane point source emissions from animal agriculture and waste based on new airborne measurements in the US Upper Midwest. *Journal of Geophysical Research: Biogeosciences*, 125(1), e2019JG005429. doi:10.1029/2019JG005429

Yu, X., Millet, D. B., Wells, K. C., Henze, D. K., Cao, H., Griffis, T. J., et al. (2021). Aircraft-based inversions quantify the importance of wetlands and livestock for Upper Midwest methane emissions. *Atmospheric Chemistry and Physics*, *21*(2), 951-971. doi: 10.5194/acp-21-951-2021

Geophysical Research Letters

Supporting Information for

Fossil vs. non-fossil CO sources in the US: New airborne constraints from ACT-America and GEM

Andres Gonzalez[1], Dylan B. Millet[1], Xueying Yu[1], Kelley C. Wells[1], Timothy J. Griffis[1], Bianca C. Baier[2,3], Patrick C. Campbell[4,5,6], Yonghoon Choi[7], Joshua P. DiGangi[7], Alexander Gvakharia[8], Hannah Halliday[7], Eric A. Kort[8], Kathryn McKain[2,3], John Nowak[6], and Genevieve Plant[8]

[1]Department of Soil, Water, and Climate, University of Minnesota, Saint Paul, MN, USA. [2]Cooperative Institute for Research in Environmental Sciences (CIRES), University of Colorado, Boulder, CO, USA. [3]Global Monitoring Laboratory, National Oceanic and Atmospheric Administration, Boulder, CO, USA. [4]Center for Spatial Information Science and Systems, George Mason University, Fairfax, VA, USA. [5]Cooperative Institute for Satellite Earth System Studies (CISESS), [6]Air Resources Laboratory, National Oceanic and Atmospheric Administration, College Park, MD, USA. [7]NASA Langley Research Center, Hampton, VA, USA. [8]Department of Climate and Space Sciences and Engineering, University of Michigan, Ann Arbor, MI, USA.

Contents of this file

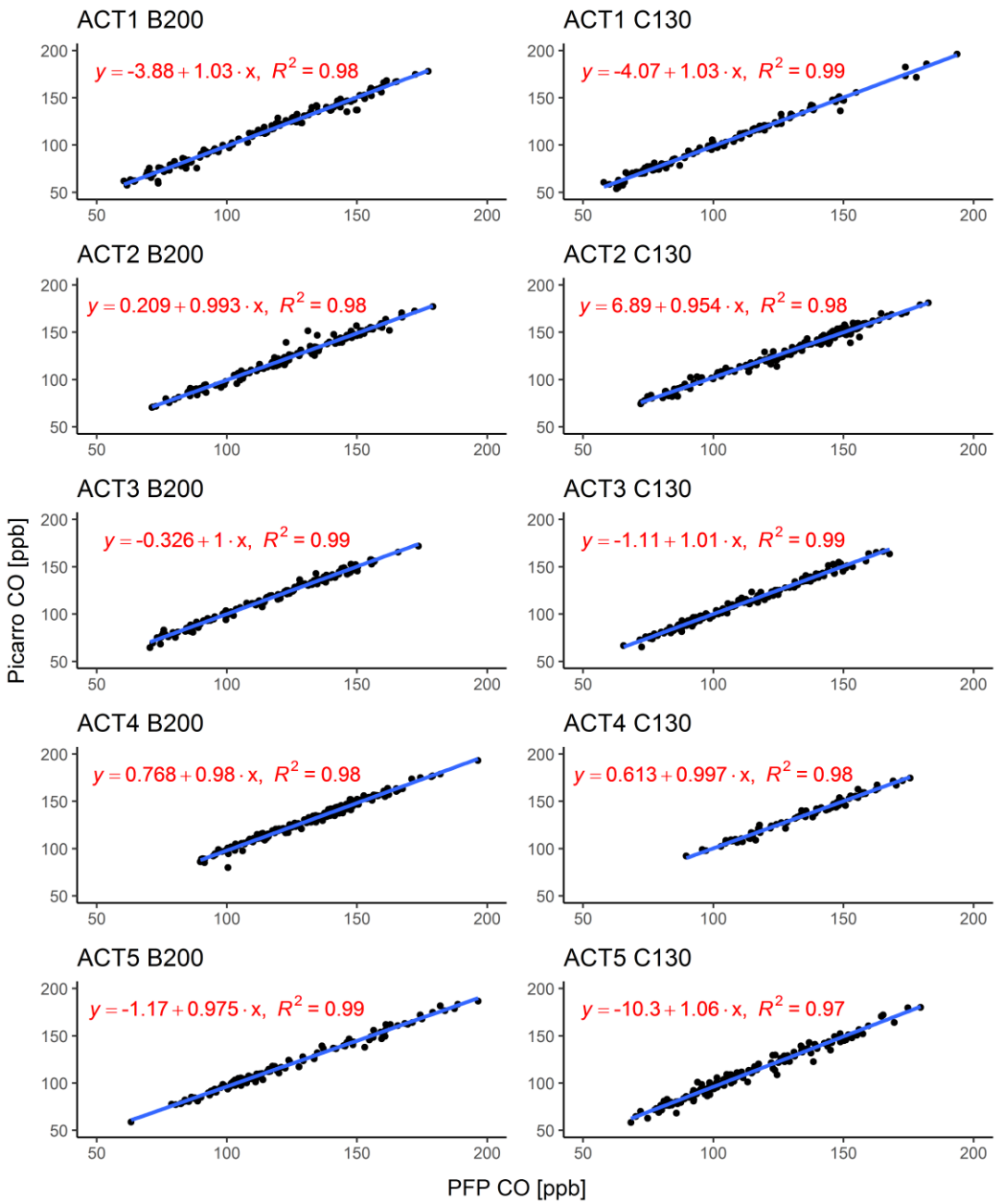

Figure S1. Intercomparison of ACT-America airborne CO measurements. In situ measurements by Picarro CRDS are plotted against PFP flask measurements on-board the Beechcraft B200 King Air (left column) and C-130H Hercules (right column) aircraft for each ACT-America deployment.

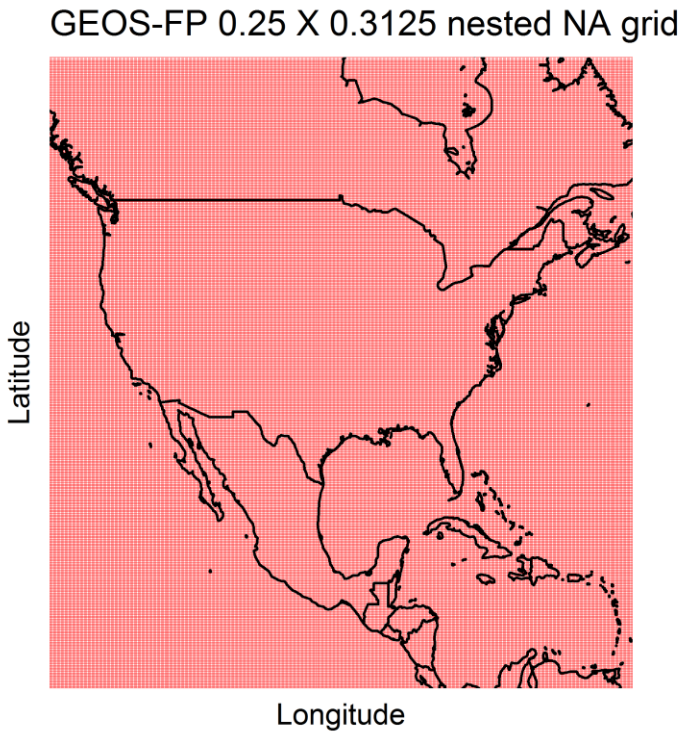

Figure S2. North American nested domain employed for GEOS-Chem simulations.

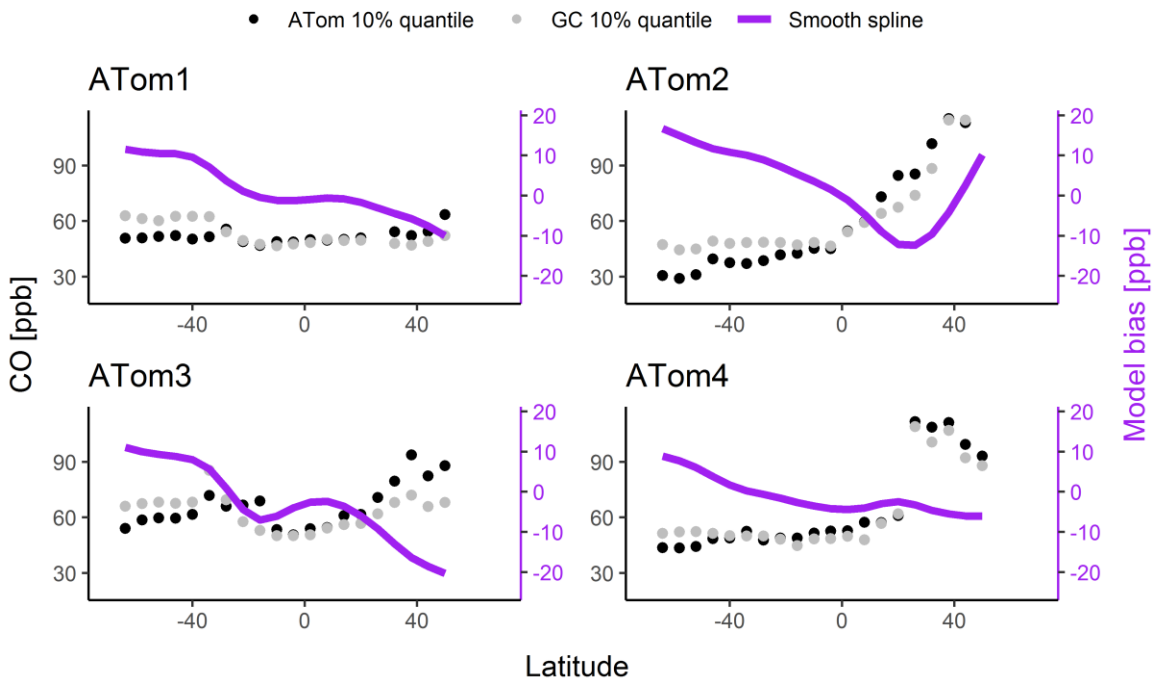

Figure S3. Correction of the GEOS-Chem CO background based on aircraft measurements from the four ATom deployments. Plotted are observed tropospheric CO mixing ratios over the remote Pacific Ocean averaged by six-degree latitude bins (black) along with the corresponding model values (grey). Data shown are restricted to 0-8 km above sea level, 80°S-56°N, and 160°E-145°W (Northern Hemisphere) or 100°W-145°W (Southern Hemisphere). Purple lines show the model-measurement mismatch as a smooth spline fit to the 0.1 quantile difference.

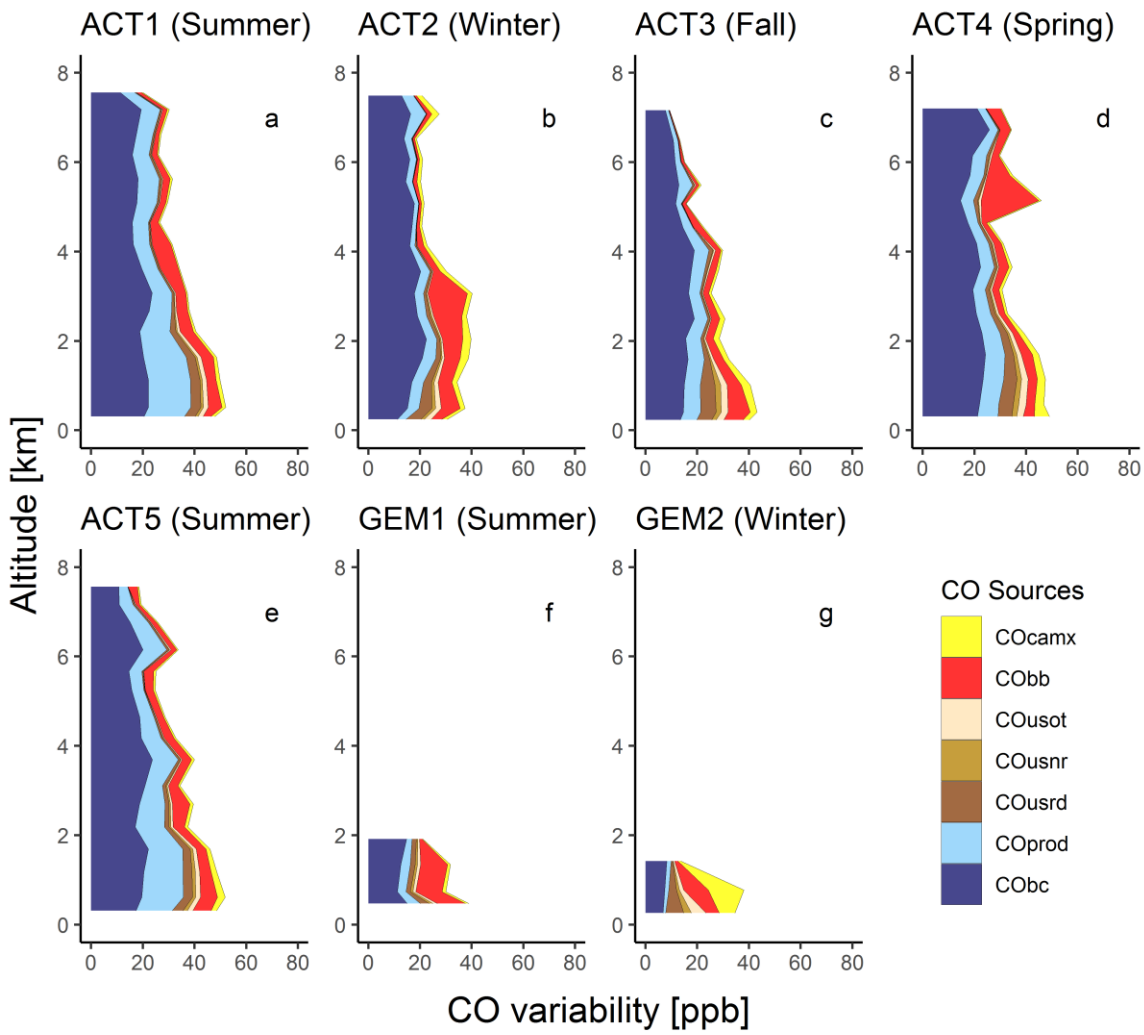

Figure S4. Sources of CO variability over the eastern US. Plotted is the standard deviation for individual tagged CO tracers based on output from the optimized GEOS-Chem simulation along the ACT-America and GEM flight tracks. CO_{bc}: CO transported from outside North America. CO_{usrd}, CO_{usnr}, CO_{usot}: anthropogenic CO emitted from US on-road, non-road, and other sources. CO_{camx}: anthropogenic CO emitted in Canada + Mexico. CO_{bb}: CO emitted from North American biomass burning. CO_{prod}: CO photochemically produced over North America. Standard deviation is not additive so the individual values do not sum to the total CO variability.

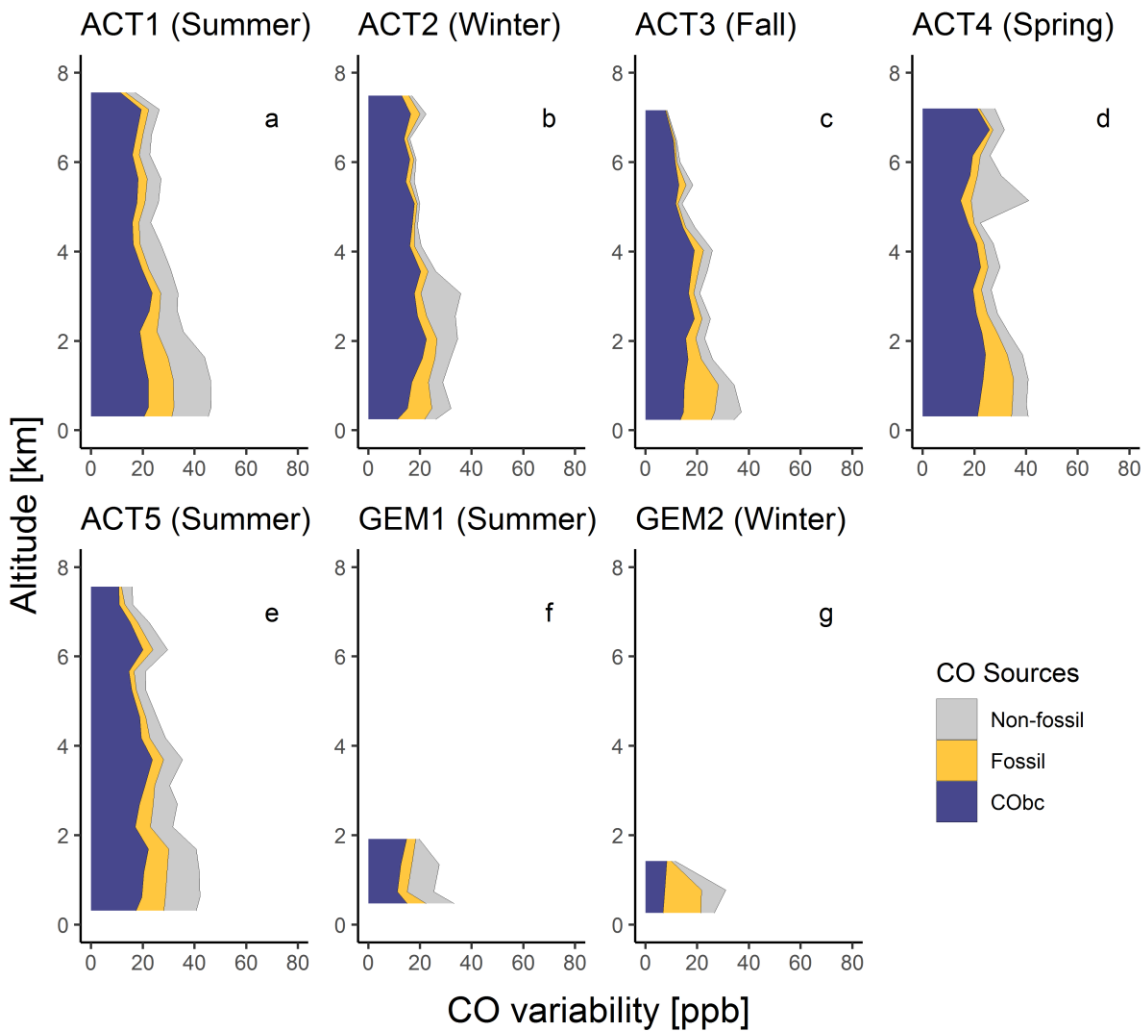

Figure S5. Sources of CO variability over the eastern US. Plotted is the standard deviation for grouped tagged CO tracers from the optimized GEOS-Chem simulation along the ACT-America and GEM flight tracks. Values are shown for non-fossil CO (from biogenic VOC oxidation plus biomass burning emissions), fossil CO (from direct emissions plus anthropogenic VOC oxidation), and CO transported from outside North America ($\mathbf{CO}_{bc}$). Standard deviation is not additive so the individual values do not sum to the total CO variability.

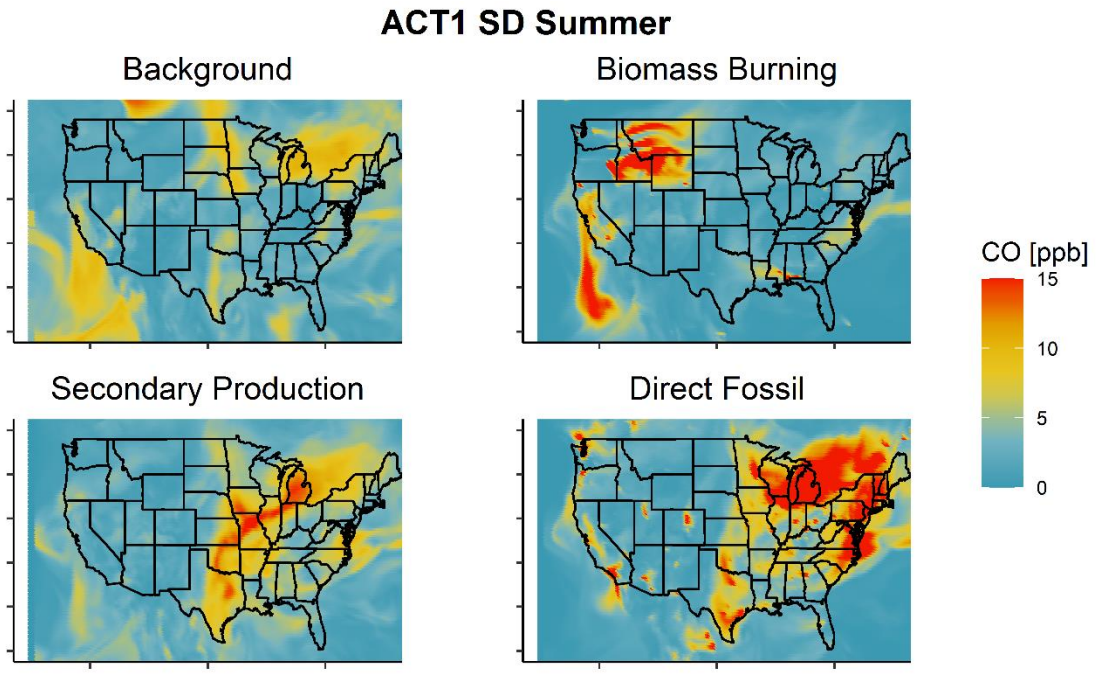

Figure S6. Temporal CO variability in the US PBL during summer. Plotted are the hourly standard deviations (SD) for background CO, biomass burning CO, secondary CO, and directly-emitted fossil fuel CO based on the optimized GEOS-Chem simulation. Data are plotted for the ACT1 timeframe (11 July to 29 August 2016).

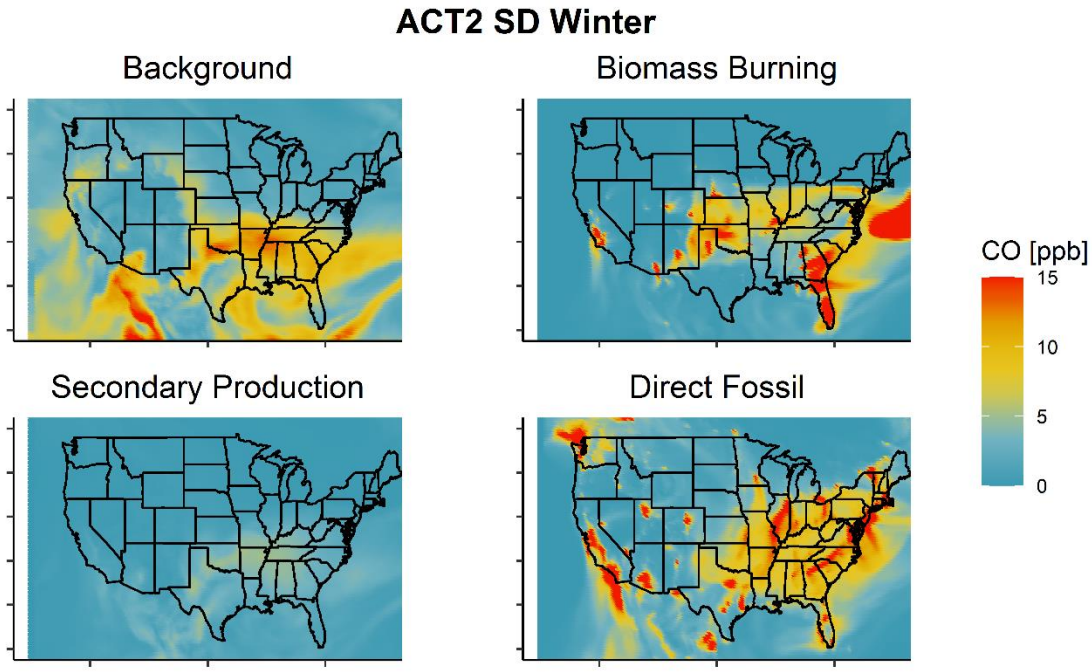

Figure S7. Temporal CO variability in the US PBL during winter. Plotted are the hourly standard deviations (SD) for background CO, biomass burning CO, secondary CO, and directly-emitted fossil fuel CO based on the optimized GEOS-Chem simulation. Data are plotted for the ACT2 timeframe (21 January to 10 March 2017).

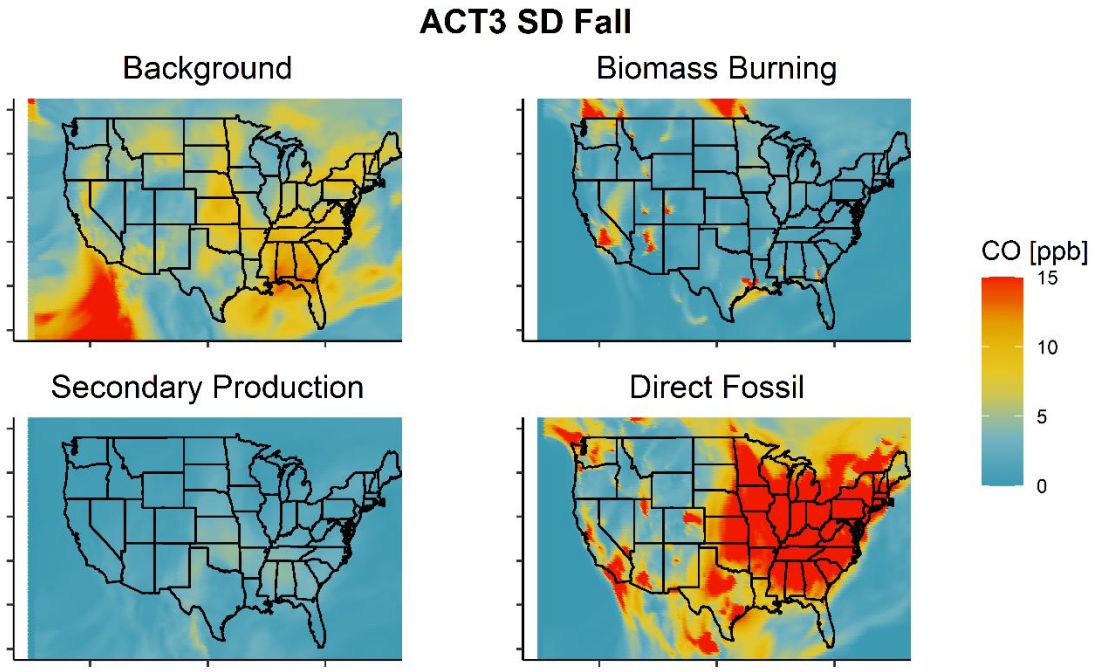

Figure S8. Temporal CO variability in the US PBL during fall. Plotted are the hourly standard deviations (SD) for background CO, biomass burning CO, secondary CO, and directly-emitted fossil fuel CO based on the optimized GEOS-Chem simulation. Data are plotted for the ACT3 timeframe (22 September to 13 November 2017).

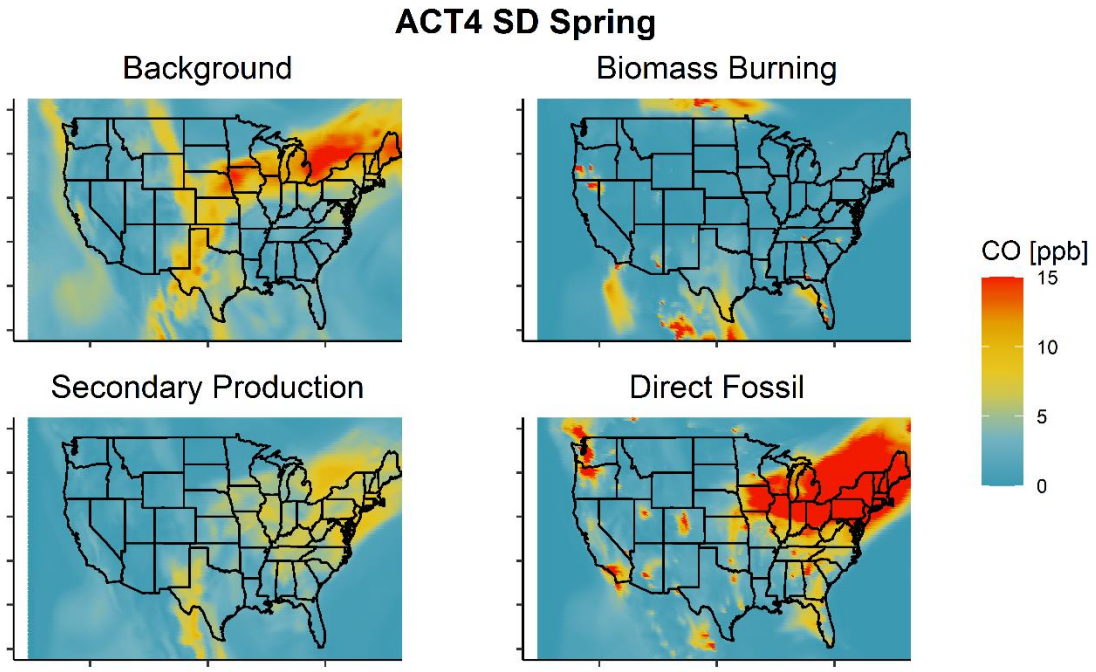

Figure S9. Temporal CO variability in the US PBL during spring. Plotted are the hourly standard deviations (SD) for background CO, biomass burning CO, secondary CO, and directly-emitted fossil fuel CO based on the optimized GEOS-Chem simulation. Data are plotted for the ACT4 timeframe (28 March to 20 May 2018).

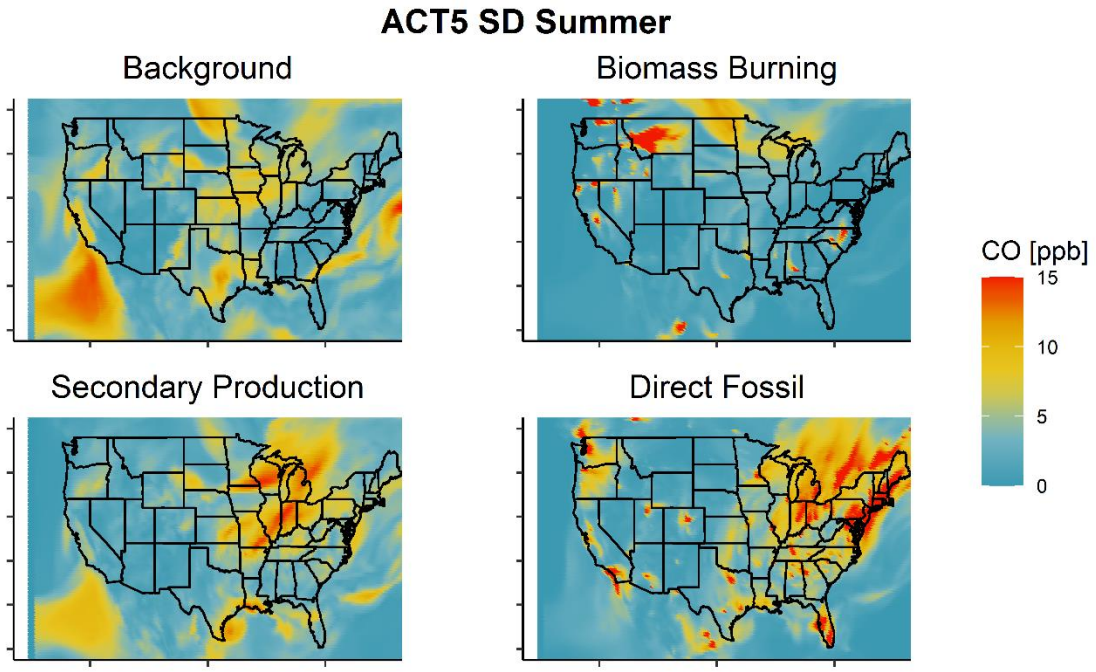

Figure S10. Temporal CO variability in the US PBL during summer. Plotted are the hourly standard deviations (SD) for background CO, biomass burning CO, secondary CO, and directly-emitted fossil fuel CO based on the optimized GEOS-Chem simulation. Data are plotted for the ACT5 timeframe (7 June to 27 July 2019).

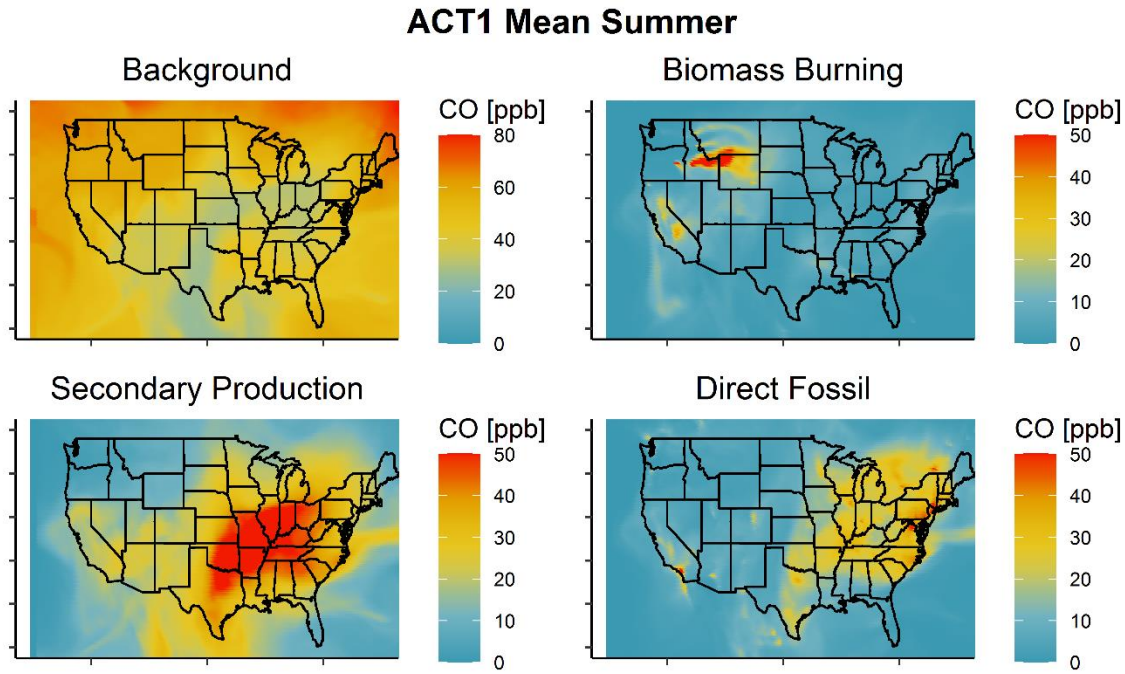

Figure S11. Contributions to the PBL CO burden over the US during summer. Plotted are the mean contributions from background CO, direct biomass burning emissions, secondary production, and direct fossil fuel emissions based on the optimized GEOS-Chem simulation. Data are plotted for the ACT1 timeframe (11 July to 29 August 2016).

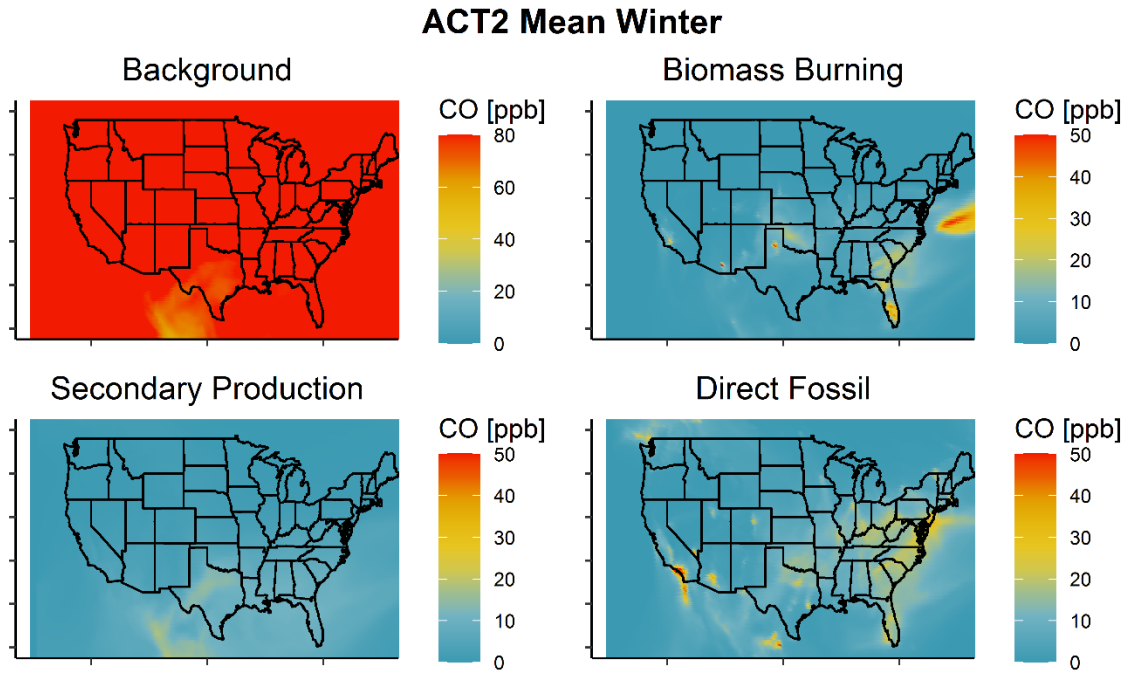

Figure S12. Contributions to the PBL CO burden over the US during winter. Plotted are the mean contributions from background CO, direct biomass burning emissions, secondary production, and direct fossil fuel emissions based on the optimized GEOS-Chem simulation. Data are plotted for the ACT2 timeframe (21 January to 10 March 2017).

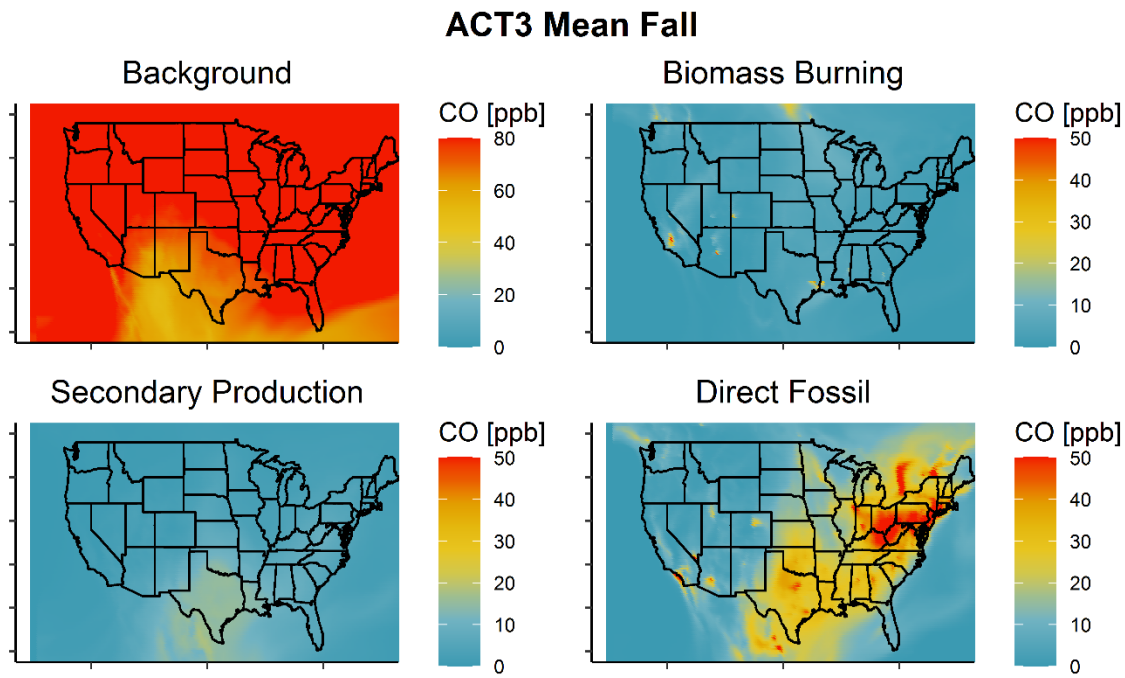

Figure S13. Contributions to the PBL CO burden over the US during fall. Plotted are the mean contributions from background CO, direct biomass burning emissions, secondary production, and direct fossil fuel emissions based on the optimized GEOS-Chem simulation. Data are plotted for the ACT3 timeframe (22 September to 13 November 2017).

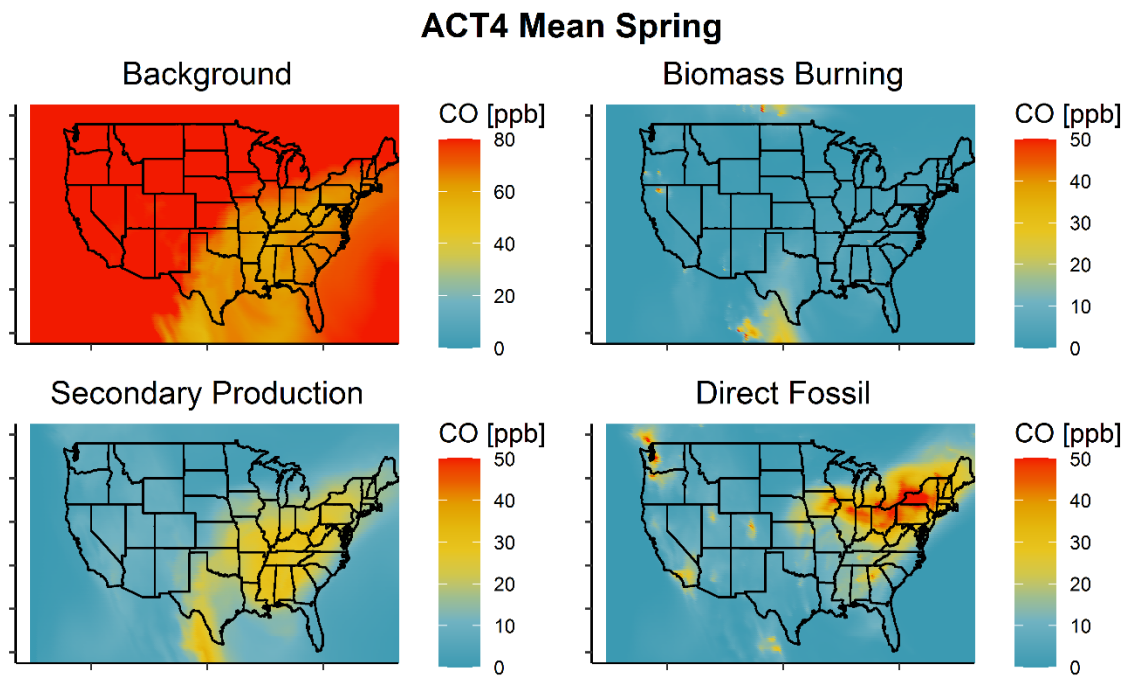

Figure S14. Contributions to the PBL CO burden over the US during spring. Plotted are the mean contributions from background CO, direct biomass burning emissions, secondary production, and direct fossil fuel emissions based on the optimized GEOS-Chem simulation. Data are plotted for the ACT4 timeframe (28 March to 20 May 2018).

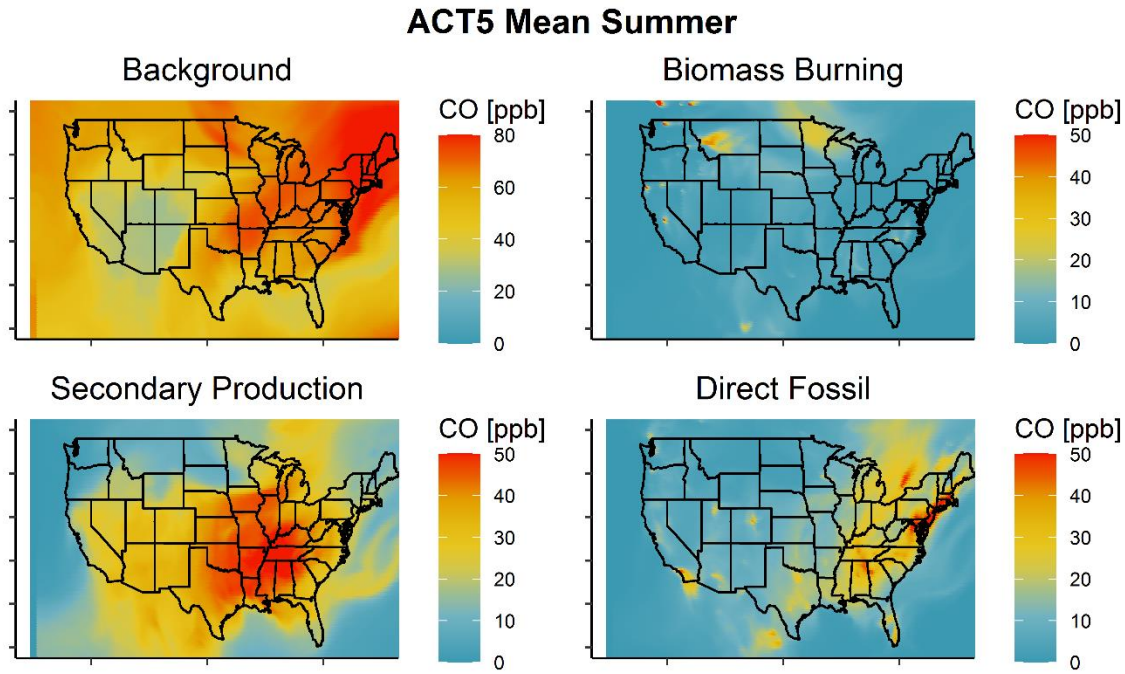

Figure S15. Contributions to the PBL CO burden over the US during summer. Plotted are the mean contributions from background CO, direct biomass burning emissions, secondary production, and direct fossil fuel emissions based on the optimized GEOS-Chem simulation. Data are plotted for the ACT5 timeframe (7 June to 27 July 2019).

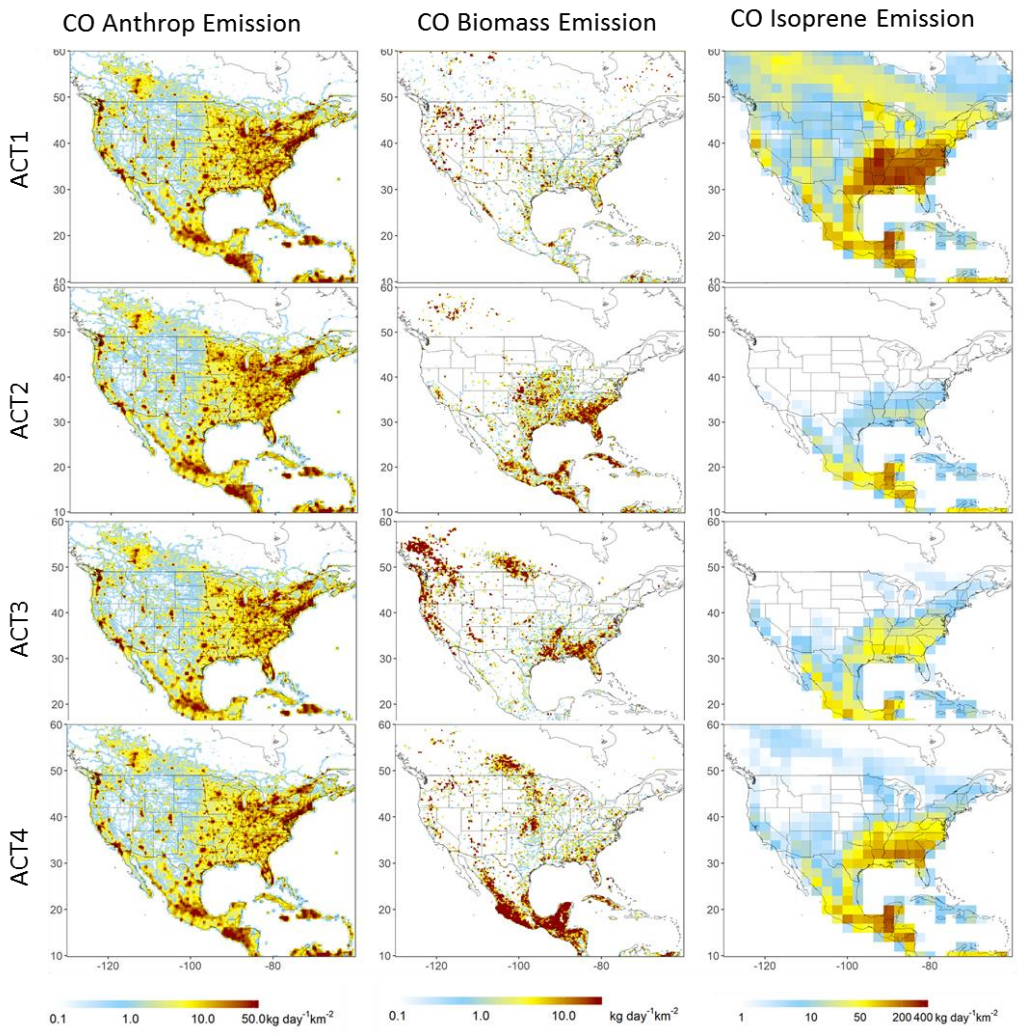

Figure S16. North American CO sources based on the prior inventories employed in this work. Left column: CO directly emitted from anthropogenic sources. Middle column: CO emitted from open burning. Right column: biogenic emissions of isoprene, a key CO precursor.

Table S1. Timeframe and flight hours for the ACT-America and GEM airborne campaigns.

Campaign	Year	Season	Start Date	End Date	Flight Hours
ACT1	2016	Summer	11 July	29 August	218
ACT2	2017	Winter	21 January	10 March	210
ACT3	2017	Fall	22 September	13 November	192
ACT4	2018	Spring	28 March	20 May	197
ACT5	2019	Summer	7 June	27 July	183
GEM1	2017	Summer	12 August	24 August	40
GEM2	2018	Winter	17 January	28 January	36

Table S2. Statistical comparison of CO mixing ratios from the prior and optimized GEOS-Chem simulations against independent airborne observations from the ACT5, GEM1, and GEM2 campaigns.

	RMSE[1] (ppb)		*R*		*Bias Mean (ppb)*	
	Prior	Post	Prior	Post	Prior	Post
ACT5 (summer)	28.2	23.2	0.51	0.57	14.0	7.8
GEM1 (summer)	57.8	35.8	0.23	0.06	48.4	12.5
GEM2 (winter)	60.9	59.1	0.36	0.32	21.9	11.8

[1] Root mean square error.

Table S3. Seasonal CO source optimization performed separately for the C-130H and B200 ACT-America datasets.

	Aircraft	CO_{usnei}		CO_{prod_voc}		Intercept	VIF[2]	RMSE (ppb)[3]		*R*		*Bias Mean*	
		Scale factor	Mean (ppb)	Scale factor	Mean (ppb)			Prior	Post	Prior	Post	Prior	Post
ACT1 (summer)	B200	0.54 ± 0.05[1]	13.1	0.96 ± 0.02	25.4	0.09 ± 0.3	3.37	26.2	16.2	0.76	0.81	17.7	0.4
	C-130H	0.87 ± 0.09	13.4	0.74 ± 0.02	25.3	8.28 ± 0.3	2.74	26.6	17.3	0.74	0.80	17.4	2.1
ACT2 (winter)	B200	0.86 ± 0.04	13.4			0.43 ± 0.4 4		21.7	16.7	0.66	0.65	14.3	0.4
	C-130H	0.67 ± 0.04	11.8			5.5 ± 0.48		21.0	13.7	0.75	0.77	16.0	3.8
ACT3 (fall)	B200	0.65 ± 0.04	17.5			6.4 ± 0.6		13.6	14.4	0.79	0.75	2.1	6.1
	C-130H	0.79 ± 0.03	15.7			4.2 ± 0.41		13.0	13.6	0.79	0.76	3.2	4.2
ACT4 (spring)	B200	0.76 ± 0.02	15.6			-4.5 ± 0.44		17.8	17.5	0.63	0.59	7.8	-4.4
	C-130H	0.65 ± 0.03	20.29			2.61 ± 0.61		18.8	16.0	0.71	0.68	11.3	2.8

[1] Stated uncertainties reflect 95% confidence intervals computed through bootstrap resampling.
[2] Variance inflation factor.
[3] Root mean square error.

Table S4. Seasonal CO source optimization performed with and without ATom-based boundary condition correction.

	CO_{bc}	CO_{usnei}		CO_{prod_voc}		Intercept	VIF[2]	RMSE (ppb)[3]		*R*		*Bias Mean*	
		Scale factor	Mean (ppb)	Scale factor	Mean (ppb)			Prior	Post	Prior	Post	Prior	Post
ACT1 (summer)	Corrected	0.66 ± 0.05[1]	13.2	0.91 ± 0.03	25.4	-0.2 ± 0.3	3.1	26.4	16.8	0.75	0.81	17.6	-2.5
	Uncorrected	0.69 ± 0.05	13.22	0.85 ± 0.02	25.4	2.7 ± 0.3	2.1	26.4	17.0	0.75	0.80	11.7	-1.2
ACT2 (winter)	Corrected	0.79 ± 0.03	12.77			1.8 ± 0.4		21.4	15.5	0.69	0.69	14.8	1.7
	Uncorrected	0.85 ± 0.03	12.77			-4.3 ± 0.3		21.4	15.5	0.69	0.74	14.8	-4.2
ACT3 (fall)	Corrected	0.69 ± 0.03	16.77			5.5 ± 0.5		13.4	14.2	0.79	0.75	2.5	5.5
	Uncorrected	0.66 ± 0.03	16.77			6.7 ± 0.5		13.4	14.7	0.79	0.75	2.6	6.7
ACT4 (spring)	Corrected	0.74 ± 0.02	16.94			-2.7 ± 0.4		18.1	17.0	0.65	0.61	8.8	-2.6
	Uncorrected	0.75 ± 0.02	16.94			-3.2 ± 0.4		18.1	17.2	0.65	0.60	8.8	-3.0

[1] Stated uncertainties reflect 95% confidence intervals computed through bootstrap resampling
[2] Variance inflation factor.
[3] Root mean square error.

Table S5. Seasonal CO source optimization for ACT1-ACT4 with alternative tracer groupings: 1) CO_{usnei} and 2) the sum of all other regional source tracers ($\mathrm{CO}_{prod\_voc} + \mathrm{CO}_{prod\_oth} + \mathrm{CO}_{camx} + \mathrm{CO}_{bb}$).

	CO_{usnei}		$\mathrm{CO}_{prod_{voc}+bb+can}$		Intercept	VIF[2]	RMSE[3] (ppb)		*R*		*Bias Mean*	
	Scale factor	Mean (ppb)	Scale factor	Mean (ppb)			Prior	Post	Prior	Post	Prior	Post
ACT1 (summer)	0.58 ± 0.05[1]	13.2	0.96 ± 0.02	26.7	-0.4 ± 0.3	2.9	26.4	16.6	0.75	0.81	17.6	-0.3
ACT2 (winter)	0.85 ± 0.03	12.77	0.7 ± 0.07	7.1	3.1 ± 0.5	1.1	21.4	15.6	0.69	0.70	14.8	3.1
ACT3 (fall)	0.82 ± 0.03	16.77	0.55 ± 0.01	14.6	5.5 ± 0.5	1.2	13.4	15.9	0.79	0.76	2.5	10.1
ACT4 (spring)	0.70 ± 0.02	16.94	1.1 ± 0.05	12.6	-3.6 ± 0.5	1.4	18.1	17.2	0.65	0.61	8.8	-3.6

[1] Stated uncertainties reflect 95% confidence intervals computed through bootstrap resampling
[2] Variance inflation factor.
[3] Root mean square error.